POLITECNICO
MILANO 1863

SCUOLA DI INGEGNERIA INDUSTRIALE
E DELL'INFORMAZIONE

Advanced Online Diagnostics for Automotive Lithium Batteries

Tesi di Laurea Magistrale in
Electrical Engineering - Ingegneria Elettrica

Author: **Alessandra Geroni**

Student ID: 10769096
Advisor: Prof. Luigi Piegari
Academic Year: 2025 - 26

Abstract

The energy transition has become one of the most prominent topics in recent years, and sustainable transportation is among the sectors most affected by these changes. In this context, electric mobility is rapidly evolving toward greater efficiency and technological advancement. Consequently, there is a growing need for increasingly sophisticated battery management systems (BMS) capable of accurately estimating the state of health (SOH) and state of charge (SOC) of batteries in real time.

Several highly effective diagnostic methods exist, such as electrochemical impedance spectroscopy (EIS), which are typically conducted offline using highly precise laboratory instrumentation and require relatively long acquisition time to ensure accuracy. These aspects limit the applicability of the method in real driving conditions, preventing online estimation of battery diagnostic parameters.

This thesis investigates the implementation of online diagnostic tools for lithium-ion batteries (LIBs), focusing in particular on two chemistries: nickel manganese cobalt (NMC) and lithium iron phosphate (LFP). The selection of these chemistries is motivated by their widespread adoption in the automotive sector. The experimental protocol was conducted using dynamic power profiles derived from the worldwide harmonized light vehicles test procedure (WLTP), adapted according to the specifications of three selected vehicles.

The core contribution of this work is the validation of online EIS estimation through a wavelet-based approach. This method enables the application of the wavelet transform (WT) to WLTP power profiles to extract impedance-related information without interrupting normal battery operation.

Furthermore, a dedicated investigation on LFP cells was conducted using differential voltage analysis (DVA). Two methods were evaluated for the identification of an electrochemical peak in the $dV/dSOC$ profile derived under real driving conditions. The results obtained from both approaches were consistent, allowing the identification of the electrochemical signature of the cell and the corresponding SOC.

The results confirm a strong correlation between the impedance estimated through wavelet

analysis and that obtained from laboratory measurements. In conclusion, the integration of online EIS and DVA represents a reliable multimodal diagnostic framework that significantly enhances the monitoring capabilities of next-generation BMS, ensuring high levels of safety and reliability for automotive battery packs.

Keywords: lithium-ion batteries (LIBs); online eletrochemical impedance spectroscopy (EIS); wavelet transform (WT); differential voltage analysis (DVA); peak identification; battery diagnostics; WLTP driving cycles; battery management systems (BMS).

Abstract in lingua italiana

La transizione energetica è uno dei temi di maggiore rilievo degli ultimi anni e tra i settori più influenzati da tali cambiamenti vi è il trasporto sostenibile. In questo contesto si sviluppa la mobilità elettrica, che mira a diventare sempre più efficiente e tecnologicamente avanzata. A tal proposito cresce la necessità di sistemi di gestione della batteria (BMS) sempre più sofisticati, in grado di stimare accuratamente e in tempo reale lo stato di salute (SOH) e lo stato di carica (SOC) delle batterie.

Esistono diversi metodi diagnostici molto efficaci, come la spettroscopia di impedenza elettrochimica (EIS), i quali vengono condotti tipicamente offline mediante strumentazioni di laboratorio altamente precise ed inoltre richiedono tempi relativamente lunghi per essere eseguiti con accuratezza. Tali aspetti limitano l'applicabilità del metodo in condizioni di guida reali, non consentendo una stima online dei parametri diagnostici della batteria.

Questa tesi investiga l'implementazione di strumenti di diagnostica online per batterie agli ioni di litio (LIBs), focalizzandosi in particolare su due chimiche: nickel manganese cobalto (NMC) e litio ferro fosfato (LFP). La scelta di tali chimiche è motivata dalla loro ampia diffusione nel settore automotive. Il protocollo sperimentale è stato condotto attraverso l'utilizzo di profili dinamici ricavati dal worldwide harmonized light vehicles test procedure (WLTP), adattati in funzione delle specifiche di tre veicoli selezionati.

Il nucleo della ricerca è la validazione della stima online dell'EIS attraverso un approccio basato sulla trasformata wavelet (WT). Questo metodo consente di applicare la WT ai profili di potenza WLTP ed estrarre informazioni relative all'impedenza senza interrompere il normale funzionamento della batteria.

Inoltre, è stato condotto uno studio specifico sulle celle LFP attraverso l'applicazione della differential voltage analysis (DVA). Sono stati analizzati due metodi per l'identificazione di un picco elettrochimico nella curva $dV/dSOC$ ricavata in condizioni di guida reale. I risultati ottenuti risultano coerenti tra i due approcci, permettendo l'identificazione della firma elettrochimica della cella e del relativo SOC.

I risultati confermano una forte correlazione tra l'impedenza stimata tramite analisi wavelet

e quella derivata da misure di laboratorio. In conclusione, l'integrazione tra EIS online e DVA rappresenta un framework diagnostico multimodale e affidabile che migliora significativamente le capacità di monitoraggio della nuova generazione di BMS, garantendo elevati livelli di sicurezza e affidabilità per i pacchi batteria in ambito automotive.

Parole chiave: batterie agli ioni di litio (LIBs); spettroscopia di impedenza elettrochimica (EIS) online; trasformata wavelet (WT); analisi della tensione differenziale (DVA); identificazione del picco; diagnostica delle batterie; cicli guida WLTP; sistemi di gestione della batteria (BMS).

Abbreviations

BMS	Battery Management System
CC	Constant Current
CEI	Cathode Electrolyte Interphase
CPE	Constant Phase Element
CV	Constant Voltage
CWT	Continuous Wavelet Transform
DVA	Differential Voltage Analysis
DWT	Discrete Wavelet Transform
ECM	Equivalent Circuit Model
EIS	Electrochemical Impedance Spectroscopy
EV	Electric Vehicle
FT	Fourier Transform
GEIS	Galvanostatic Electrochemical Impedance Spectroscopy
LIB	Lithium-Ion Battery
OCV	Open Circuit Voltage
SEI	Solid Electrolyte Interface
SOC	State of Charge
SOH	State of Health
WLTC	Worldwide Harmonized Light Vehicles Test Cycle
WLTP	Worldwide Harmonised Light Vehicles Test Procedure
WT	Wavelet Transform

Contents

Introduction

Background and motivation

In recent years, the world has been increasingly moving towards a vision of a sustainable future by developing advanced and environmentally friendly technologies. LIBs exhibit an optimal combination of high energy and power density, an attribute that makes them currently unrivaled in both stationary and mobile applications. The latter category encompasses a wide range of devices, from smaller ones such as smartphones and laptops to larger ones such as EVs and grid-scale battery energy storage systems (BESS). An increase in the adoption of electric vehicles and a corresponding decrease in petrol-powered vehicles, would cause a drastic reduction of greenhouse gas emissions. Road transportation represents a significant source of pollution and, for this reason, it is crucial to move towards fully electric mobility. The growing adoption of EVs has led to increased interest in advanced diagnostic methods for lithium-ion batteries. Among these, EIS represents an important tool for monitoring battery health and internal electrochemical dynamics. However, nowadays traditional EIS measurements are performed offline, limiting real-time applications in BMS. These measurements are time-consuming and generally conducted while the vehicle is turned off, leading to underestimating the importance of such testing, despite the fact that it provides valuable information regarding battery state during its life. Currently, EVs still represent a minority compared to combustion engine vehicles, and among the various aspects that concern users is the battery pack's range on long journeys. In this regard, it would be highly useful and advantageous to be able to assess the state of a vehicle's LIBs online, while the vehicle is in operation, thus enabling access to information on the battery's SOH at any moment and in a considerably faster manner. This thesis proposes an experimental validation of LIB EIS estimation through the use of WTs. Furthermore, this project also describes DVA as a diagnostic method for battery systems. In the literature it is possible to find how this analysis has been predominantly employed for SOH estimation but an efficient identification of electrochemical signatures under real driving conditions has not been reported; in this project, the parameters influencing the DVA results are highlighted, and subsequently two methodologies to select

the meaningful peak of the dynamic profiles is presented.

Research objectives and contributions

Electrochemical impedance spectroscopy is generally performed offline using various methodologies and dedicated instrumentation, which make the overall process time-consuming. Moreover, performing this type of measurement on vehicles often requires disassembling the cell from the battery pack. Moreover, this procedure is typically carried out during maintenance operations and it is therefore not performed continuously, leading to limited monitoring. The investigation of impedance spectroscopy through offline estimation requires controlled operating conditions, typically a fixed SOC, as well as extensive and complex post-processing. This diagnostic tool is fundamental, as the analysis of the resulting impedance spectrum allows conclusions to be drawn regarding the battery degradation behavior over time. Lithium-ion batteries are affected by multiple degradation phenomena that progressively reduce their performance; through impedance spectra, it is possible to identify such aspects and gain insight into the processes occurring within the cell. Identifying internal battery behavior enables continuous monitoring of the SOH over time and, potentially, the detection of abnormal operating conditions. In this regard, impedance analysis is vital throughout the device lifetime and should ideally be performed on a frequent basis. As previously highlighted, offline impedance identification is computationally and temporally expensive and does not provide real-time information. These limitations emphasize the importance of investigating online methods for EIS identification that do not require dedicated hardware and that allow diagnostic information to be obtained while the vehicle is in operation. In this thesis, such an approach is validated by comparing experimental EIS data obtained through offline measurements with EIS results derived using the WT. The study and application of wavelet-based methods were carried out in collaboration with researcher Roberta Di Fonso. Subsequently, the DVA is employed using two different methodologies to accurately detect the electrochemical peak under real driving conditions in an LFP cell. These electrochemical signatures constitute characteristic features of the battery chemistry, and their analysis makes it possible to extract information regarding the internal condition of the battery. This thesis aims to validate and present effective methodologies for the identification of the key battery diagnostic parameters within the context of LIB performances.

Thesis outline

This thesis is structured as follows:

- **Chapter 1** provides a theoretical background on LIBs, toward the selection of the two chemistries investigated in this work. In addition, the main aging mechanisms affecting the cells are presented and discussed from both electrochemical and application-oriented perspectives. The theoretical foundations and diagnostic applications of EIS are then introduced, followed by an overview of the current challenges associated with online impedance estimation.
- **Chapter 2** shows a classification of the vehicles selected for this study, describing the most commonly used battery configurations. Subsequently, the WLTP driving cycle is presented together with the mathematical criteria adopted to derive the power profiles associated with each selected vehicle.
- **Chapter 3** presents a representation of the laboratory setup used for the experimental tests, presenting the instrumentation involved and the testing protocols adopted for EIS evaluation. In the final part, the diagnostic method developed through DVA applied to the LFP cell is described.
- **Chapter 4** introduces a theoretical introduction to the concept of the WT in the field of power signal analysis, describing its main principles and advantages for the considered application. The use of this tool under dynamic power profile excitation is then explained, and the comparison framework between conventional offline EIS and wavelet-based impedance estimation is introduced.
- **Chapter 5** describes the comparison between the experimental results from the laboratory and the wavelet-based estimation, constituting the central element for the validation of the proposed methodology. Moreover it explains how to find a meaningful electrochemical signature using DVA through two different methods applied to an LFP cell.
- **Chapter 6** summarizes the key outcomes of the study, highlights potential application scenarios and opens the way for future research developments.

1 | Lithium-Ion Battery technology and diagnostics

1.1. Fundamentals of Lithium-Ion Battery electrochemistry

The adoption of rechargeable batteries has grown significantly, driven largely by the rapid development and increasing deployment of EVs, where batteries represent the primary onboard energy source. Several battery chemistries are currently available; however, lithium-ion batteries are among the most suitable options for EV applications. Compared with other technologies such as lead–acid batteries, nickel–cadmium (Ni–Cd) batteries, and nickel–metal hydride (Ni-MH) batteries, LIBs offer superior performance in terms of efficiency and power/energy density. Another key advantage for EV deployment is their relatively wide operating temperature range, which must be carefully considered when designing a battery pack for automotive applications. Figure 1.1 summarizes the performance ranges of the main battery technologies currently considered for EV applications using Ragone plots. In particular, Figure 1.1 (a) compares specific energy and volumetric energy density, highlighting that LIBs enable compact cell designs while delivering improved driving range compared with alternative chemistries. Figure 1.1 (b) compares specific energy density and specific power density. In both plots, target values for future EV energy- and power-density goals are also reported. Emerging "beyond-LIB" technologies, including sodium-ion and solid-state batteries, still exhibit limitations that make them insufficiently mature for widespread EV adoption; for this reason, they are shown as semi-transparent regions [1].

Each battery cell is composed of four main components: two electrodes (anode and cathode), an electrolyte, and a separator. The electrodes consist of current collectors coated with a mixture of active materials, conductive additives, and binders, whose purpose is to enhance electrical conductivity and mechanical stability. Lithium ions (Li^+) migrate between the electrodes through the electrolyte, which is typically a solution of a lithium salt

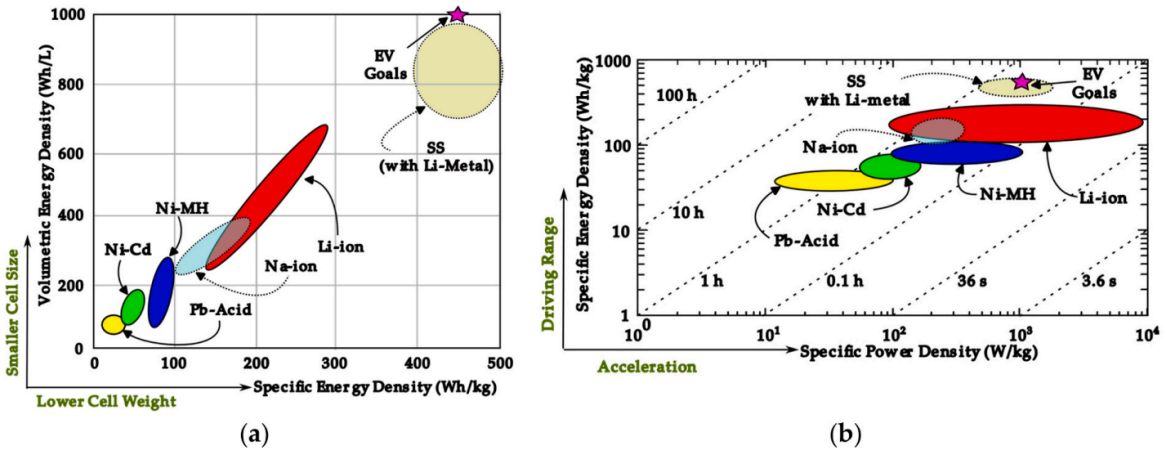

Figure 1.1: Ragone plots illustrating the energy and power characteristics of emerging battery technologies for EVs. (a) Specific energy density vs volumetric energy density. (b) Specific power density vs specific energy density [1].

dissolved in an organic solvent. Moreover, a microporous polymer membrane, referred to as the separator, is placed between the electrodes to prevent internal short circuits between the anode and the cathode. The separator is selectively porous: it allows the transport of Li^+ ions while simultaneously blocking the passage of electrons (e^-). Consequently, e^- flow through the current collectors and the external circuit, where electrical loads can be supplied or, conversely, where the battery can be recharged. The operating modes of a LIB are illustrated in Figure 1.2. During the charging process (Figure 1.2 (b)), lithium ions tend to de-intercalate from the cathode, which represents their stable chemical state, migrate through the electrolyte and the separator membrane, and intercalate into the anode. Simultaneously, electrons flow through the external circuit in the opposite direction in order to maintain electroneutrality within the cell. In contrast, during the discharge process (Figure 1.2 (a)), the operating mechanism is reversed. In this condition, the battery delivers electrical energy to an external load: electrons flow from the anode to the cathode through the external circuit, while Li^+ ions migrate back toward the cathode, returning to their stable chemical state.

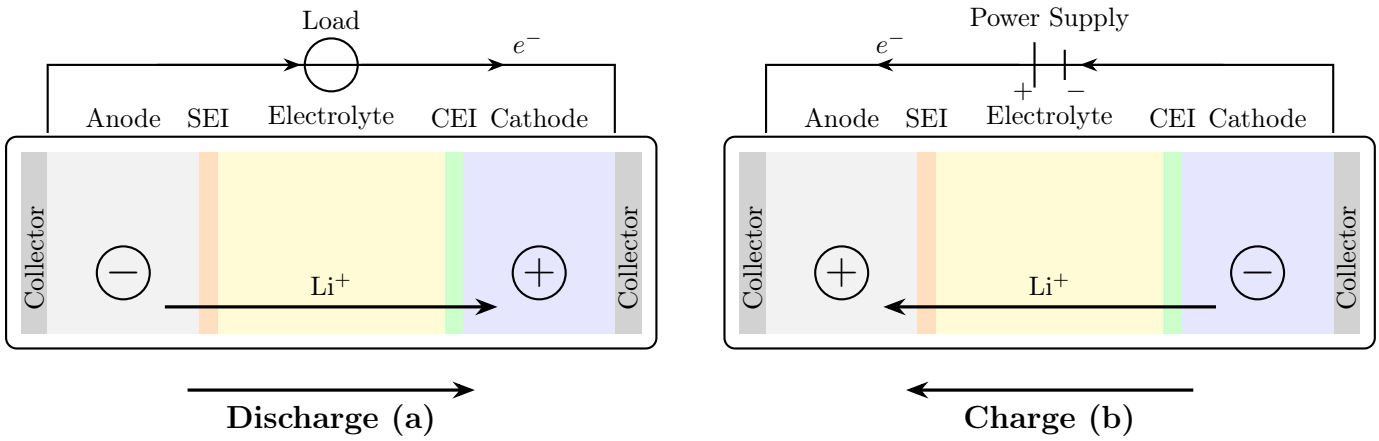

Figure 1.2: Simplified schematic representation of lithium-ion battery operation during discharge (a) and charge (b).

As shown in Figure 1.2, the battery polarity depends on the operating mode. During discharge, the anode acts as the negative electrode, whereas the cathode is the positive electrode. This occurs because, in the discharge phase, oxidation takes place at the anode side and so the electrons are released, while at the cathode side the reduction occurs and the electrons are consumed. During charging, the situation is reversed. The de-intercalation and intercalation processes of Li^+ are inherently reversible phenomena. Nevertheless, during the initial charge–discharge cycles, a loss of active material is commonly observed due to the formation of two interfacial layers that develop on the electrodes. In particular, the formation of the solid electrolyte interphase (SEI) on the anode and the cathode electrolyte interphase (CEI) on the cathode plays a crucial role in the battery lifetime. SEI is a passivating layer that forms during the first charge–discharge cycles due to the decomposition of the electrolyte on the anode surface at low potentials. This surface allows the transport of Li^+ ions while simultaneously blocking electrons, thereby preventing further electrolyte decomposition. In this way, it stabilizes the electrode–electrolyte interface. This layer has a protective function and it is essential for the proper operation of the cell. CEI, on the other hand, is a surface layer that forms on the cathode as a result of reactions between the electrolyte and the cathode material at high voltages. Similarly to SEI, this interface plays a stabilizing role for the cathode by reducing parasitic reactions and limiting the dissolution of transition metals. In contrast to the SEI, this interfacial layer does not systematically form during the initial charge–discharge cycles. Its formation occurs only when high electrode potentials are attained, triggering electrolyte decomposition reactions at the cathode surface. However, both interphases consume active electrode material, leading to an increase in internal resistance and a gradual loss of

capacity over time.

Inside the battery different electrochemical reactions occur which describe the phenomena of intercalation and de-intercalation of lithium. Within the cell, the two electrodes are governed by the so-called half-cell reactions, one occurring during discharge and the other during charge, in which lithium ions and electrons are involved. These reactions are fundamental to understanding the local phenomena taking place at the electrode interfaces, since the electrodes are made of different materials and therefore exhibit distinct electrochemical behaviors. The algebraic sum of these two half-cell reactions gives rise to the overall cell reaction, in which electrons and ions are eliminated through charge and mass balance. This overall reaction enables the comparison of batteries based on different chemistries, the calculation of key quantities such as cell capacity and nominal voltage, and, most importantly, the description of the electrochemical energy conversion process. The half-cell reactions reported in Table 1.1 are expressed in a generalized form and are valid for all lithium-ion battery chemistries. The term MO_2 denotes the active cathode material, where M represents a transition metal such as Ni, Mn, or Fe. Transition metal oxides possess some attractive characteristics which have made them generate a lot of interest as top candidates for LIB anode materials. They are non-toxic, possess high power density, theoretical specific capacity, are abundant in nature and have a low-cost fabrication process. The parameter x represents the molar fraction of intercalated lithium, while Δx describes the incremental amount of lithium extracted from the cathode or inserted into the electrodes during the charging and discharging processes, respectively. The term C_6 represents graphite, which is the material most commonly used as the anode in lithium-ion batteries. Carbon's microstructure, crystallinity, and morphology all have a significant effect on the nature, attributes and capacity of the lithiation compound. Different carbon materials possess varying bond-distances, with varying stacked-layer thicknesses, resulting in diverse lithiation capacities. Presently, in the electric industry, it is observed and recorded that coke or hard carbon, as an anode, possesses excellent stability of cycles, whereas graphite electrodes exhibit high energy density and excellent capacity [2].

Table 1.1: Generalized electrochemical reactions of a lithium-ion battery during charge and discharge.

Electrode	Mode	Electrochemical reaction	
Cathode	Charge	$Li_xMO_2 \longrightarrow Li_{x-\Delta x}MO_2 + \Delta x\, Li^+ + \Delta x\, e^-$	(1)
	Discharge	$Li_{x-\Delta x}MO_2 + \Delta x\, Li^+ + \Delta x\, e^- \longrightarrow Li_xMO_2$	
Anode	Charge	$C_6 + \Delta x\, Li^+ + \Delta x\, e^- \longrightarrow Li_{\Delta x}C_6$	(2)
	Discharge	$Li_{\Delta x}C_6 \longrightarrow C_6 + \Delta x\, Li^+ + \Delta x\, e^-$	
Overall reaction	Charge	$Li_xMO_2 + C_6 \longrightarrow Li_{x-\Delta x}MO_2 + Li_{\Delta x}C_6$	(3)
	Discharge	$Li_{x-\Delta x}MO_2 + Li_{\Delta x}C_6 \longrightarrow Li_xMO_2 + C_6$	

1.2. Electrochemistry overview: NMC vs LFP chemistries

The term 'lithium-ion batteries' encompasses a wide variety of chemistries, each of them offers a favourable trade-off in terms of energy density, safety, and lifetime for automotive applications. Different chemistries of LIBs show distinct energy capacity and performances, these differences must be taken into account to choose the best candidate for every application. The transition metal oxide $LiCoO_2$ (LCO) is the first and the most commercially successful form of layered transition metal oxide cathodes introduced by Goodenough [3]. This material has very important features in terms of high specific capacity, high volumetric capacity and good cycling performance. Anyway the major limitations are the high cost of cobalt (Co), the capacity fade at high current rates or during long and intensive cycling and the low thermal stability. For these reasons other types of metals (Mn, Al, Fe) have been taken into account as substitutes for Co. The substitution of cobalt with nickel (Ni) led to the development of lithium nickel oxide ($LiNiO_2$, LNO). This compound exhibits a specific capacity comparable to LCO; however, pure LNO cathodes are not considered favourable for practical applications. This limitation arises from the tendency of Ni^{2+} ions to occupy lithium sites, leading to cation disorder and consequently hindering lithium-ion diffusion within the crystal structure. In this context, partial substitution of Co with Ni has been demonstrated to be an effective strategy to mitigate cation mixing and improve electrochemical performance. At the same

time, lithium manganese oxide ($LiMn_2O_4$, LMO) exhibits several advantageous properties, primarily due to the fact that Mn is significantly less expensive and less toxic than Co or Ni. Nevertheless, its electrochemical performance is affected by structural instability, as the layered structure can transform into a spinel structure during lithium extraction. Moreover, Mn dissolution occurs during cycling, leading to the formation of Mn^{2+} ions, which are soluble in the electrolyte. This phenomenon destabilizes the SEI formed on the anode surface and it has been reported that Mn dissolution into the electrolyte increases with cell aging, contributing to capacity fade and performance degradation [4]. Continuous research efforts towards new cathode materials which result less expensive than LCO resulted in the formulation of the $Li(Ni_{0.5}Mn_{0.5})O_2$ (NMO) cathode. This material can mantain similar energy density to LCO while reducing considerably the cost. The presence of Ni allows higher Li extraction capacity to be achieved, however cation mixing can cause low diffusivity of lithium. The incorporation of Co into this compound has been shown to be highly effective in enhancing structural stability, leading to the development of ternary layered oxides such as $LiNi_xCo_yMn_zO_2$ (NMC) [5]. Among NMC chemistries $LiNi_{0.33}Co_{0.33}Mn_{0.33}O_2$ is the most used in the battery market. NMC material presents a similar structure to the other kind of cathodic compounds and provides equivalent performances to that of LCO, but it has some advantages in terms of lower raw material costs and improved thermal stability during abuse. This chemistry is designed to exploit the complementary roles of Ni, Mn and Co giving a perfect trade-off between energy density, stability and cost. However, the thermal stability of this kind of batteries have less favourable performance than other types and owing to the multiple compounds, the complexity of mixing process has also significantly enhanced in the manufacture phase.

Researchers studying for new cathode materials have developed a new class of compounds called polyanions (S, P, Si, Mo) which occupy lattice positions and increase cathode redox potential while also stabilizing its structure [6]. With the introduction of phosphate-based cathode materials, lithium iron phosphate ($LiFePO_4$, LFP) batteries have proven to be significantly safer than other chemistries such as LCO or LMO. Phosphates exhibit high structural and thermal stability under overcharge conditions and show strong resistance to elevated temperatures without undergoing decomposition. As a result, these materials are inherently less prone to thermal runaway in the event of overheating. Owing to these characteristics, LFP batteries operate over a wide temperature range, both in operation and storage, typically spanning from $-30\,^{\circ}C$ to $+60\,^{\circ}C$ and from $-50\,^{\circ}C$ to $+60\,^{\circ}C$, respectively [7]. In addition, LFP cathodes are non-toxic, more cost-effective than alternative cathode materials, and widely available due to the abundance of iron and phosphate resources. In Figure 1.3 [8], are represented the voltage curves with respect to

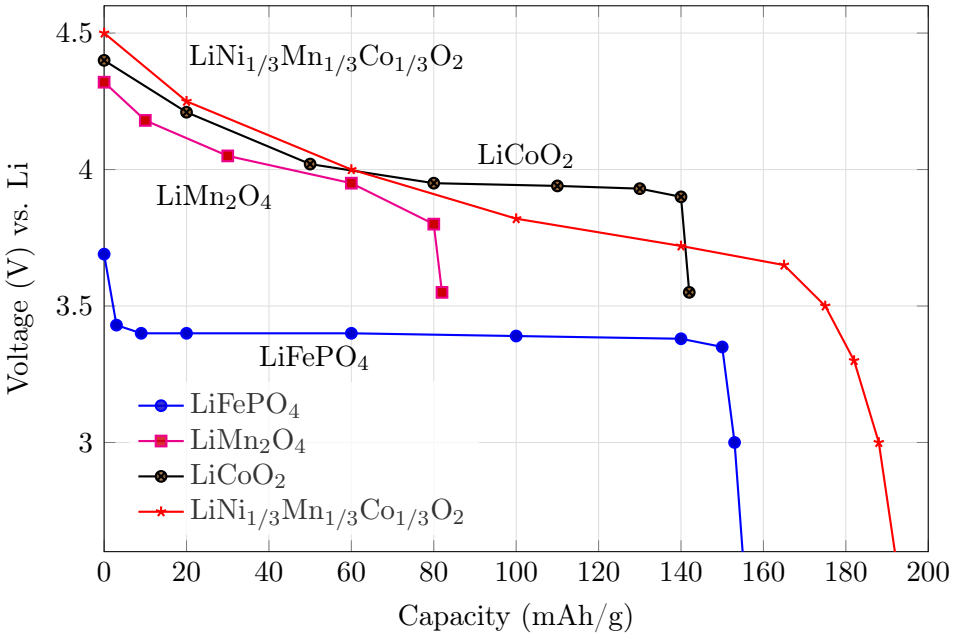

Figure 1.3: Voltage vs. capacity for several Li-ion cathode chemistries [8].

the capacity for the different chemistries. NMC chemistry exhibit superior performances in terms of capacity and operating voltage with respect to other chemistries. LFP cells exhibit a lower operating voltage compared to other lithium-ion chemistries, yet they are widely adopted and highly developed. They not only provide the required capacity and a lifetime of thousands of cycles, but also improve safety during charging. This aspect is particularly important for electric vehicles, where safety and power capability are often as critical as the energy density. These features make these two chemistries the most suitable candidates for electric vehicle applications. Their different chemical compositions lead to significant differences in performance, thermal stability, and long-term degradation behavior. The degradation mechanisms differ primarily as a consequence of their distinct chemical and structural properties. In LFP batteries, the strong iron–phosphate bond provides high electrochemical stability, thereby preventing structural breakdown under normal operating conditions. In contrast, NMC cells are more susceptible to structural changes at the electrode level, which can limit their long-term utilization. In particular, cobalt loss and transition-metal dissolution are among the main contributors to capacity fade in NMC-based batteries. The energy density of NMC batteries typically ranges from 150 to 260 Wh/kg, making them particularly suitable for applications that require high energy content within a limited volume, such as electric vehicles. Conversely, LFP batteries do not reach comparable energy density values; however, this limitation is compensated by other advantages, including longer cycle life and superior thermal stability. In conclusion, from an electrochemical perspective LFP and NMC batteries represent two different design

philosophies: LFP batteries are generally preferred for energy storage systems that require long lifetime, high stability, and enhanced safety, such as electric buses or low-cost electric vehicles, where maximizing driving range is not the primary objective. In contrast, NMC batteries are more commonly employed in high-performance electric vehicles due to their higher energy density. This aspect is particularly relevant in the automotive market, which is progressively moving toward lighter vehicles, where space saving and high output power represent two fundamental design requirements [9].

1.3. Aging mechanisms and State of Health indicators

Lithium-ion batteries degrade over time due to several factors, depending on the specific application, leading to a progressive reduction in performance and available capacity. Figure 1.4 illustrates some of the most commonly reported degradation mechanisms in Li-ion cells. Researchers have extensively investigated, and continue to investigate, battery degradation mechanisms in order to develop increasingly advanced methods for predicting the remaining useful life of batteries, which is a critical aspect in the transportation sector. Aging mechanisms are generally classified into three main categories: conductivity loss (CL), loss of lithium inventory (LLI), and loss of active material (LAM). CL describes the reduction in the ability of battery materials to conduct Li^+ and e^-. This type of degradation can be caused by binder decomposition, lithium dendrite formation, as well as changes in porosity and degradation of the separator integrity. LLI occurs mainly due to the growth of the CEI, electrolyte decomposition, and the continuous growth, decomposition, and reformation of the SEI layer. During lithiation and delithiation processes, a fraction of Li^+ is irreversibly consumed by parasitic side reactions, such as SEI formation on the negative electrode and CEI formation on the positive electrode. Lastly, LAM refers to the loss of electrochemically active material in the electrodes. This phenomenon can be induced by several factors, including lithium plating and dendrite formation, binder decomposition, corrosion of current collectors, and transition metal dissolution [10]. LAM mainly affects the positive electrodes, leading to structural disorder of the oxide lattice, transition metal ion dissolution, and surface cracking. High operating voltages and elevated temperatures significantly accelerate this degradation mechanism. Dissolved species can migrate through the electrolyte and interact with the negative electrode or precipitate back onto the positive electrode surface, ultimately resulting in a reduction of the cell capacity [11].

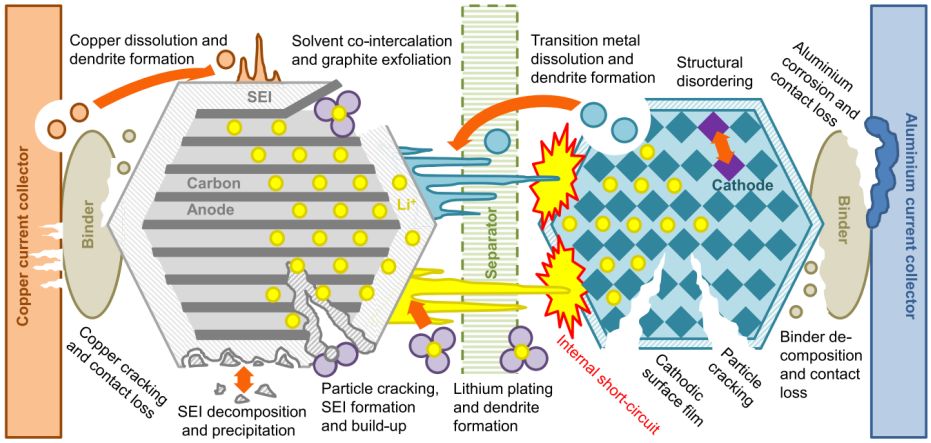

Figure 1.4: Degradation mechanisms in Li-ion cells [10]

The aforementioned aging mechanisms are accelerated and driven differently depending on the operating conditions. These conditions are generally classified into calendar aging and cycling aging. Calendar aging is defined as the degradation of lithium-ion batteries over time while they are at rest, whereas cycling aging refers to degradation caused by continuous active operation, and therefore by sustained current flow. Considering the battery of an EV as an example, calendar aging occurs when the vehicle is parked, while cycling aging takes place during driving or charging phases. Among the main contributors to cycling aging is the LLI associated with repeated lithium intercalation and deintercalation processes at the electrodes. In contrast, calendar aging is typically driven by the formation and growth of passive layers on the negative electrode under idle conditions [12]. The variables most strongly affected by calendar aging are temperature and SOC. The way in which these parameters influence the aging process is highly dependent on the battery chemistry. Several authors have described calendar aging through an Arrhenius exponential equation [13]:

$$Q_{loss}^{cal} = a \cdot e^{b \cdot \mathrm{SOC}} \cdot e^{c/T} \cdot t^{z} \tag{1.1}$$

where:
Q_{loss}^{cal} is the loss of capacity due to calendar aging [%];
a, b and c are constants that depend on the battery chemistry;
T is the temperature of the battery [K];
t is the time [s];
z is an exponential parameter that can take values between 0.5 and 1.

Equation 1.1 is largely adopted, other reserchears substitute the SOC by the open circuit

voltage (OCV), which is directly related with the former variable [14]. Cycling aging, on the other hand, depends on the operational usage of the battery, i.e. the power profile under which the battery operates, as well as on the battery chemistry and temperature. Regarding temperature, its effect on the cycling aging of lithium-ion batteries has been extensively investigated. Both excessively high and excessively low temperature levels induce accelerated degradation phenomena. Equations 1.2 and 1.3 represent the expression commonly used to model cycling aging for LFP and NMC chemistries [15].

$$Q_{loss}^{cyc} = B(C_{rate}) \cdot e^{-Ea/RT} \cdot Ah^{0.55} \tag{1.2}$$

$$Q_{loss}^{cyc} = (a \cdot T^2 + b \cdot T + c) \cdot e^{(d \cdot T + e) \cdot C_{rate}} \cdot Ah \tag{1.3}$$

where:
Q_{loss}^{cyc} is the loss capacity due to cycling aging [%];
a, b, c, d and e are constants that depend on the battery chemistry;
Ah are the ampere-hour flown in and out of the battery;
B is a pre-exponential factor;
C_{rate} is the charge/discharge current of the battery referred to its nominal capacity;
Ea is the Arrhenius activation energy $[J \cdot mol^{-1}]$;
$R = 8.314$ is the gas constant $[J \cdot mol^{-1} \cdot K^{-1}]$.

The parameter that quantifies the aging level of a battery based on the previously described aspects is the battery SOH. Equation 1.4 defines the SOH as the percentage of the nominal capacity that the battery retains after prolonged operation and multiple charge–discharge cycles. This parameter is commonly associated with either capacity fade or power fade. The former refers to the loss of usable capacity, typically expressed in ampere-hours (Ah), while the latter is related to the increase in the internal impedance of the cell.

$$SOH = \frac{Q_{\text{actual}}}{Q_{\text{nominal}}} \cdot 100 \tag{1.4}$$

A wide range of studies has investigated techniques for SOH estimation. These approaches can be broadly classified into three main categories: (1) direct measurement approaches, (2) data-driven approaches, and (3) model-based approaches:

- **Direct measurement approaches:** these methods use raw measured data to estimate SOH without reproducing the dynamic behaviour of the battery.The use of EIS as a tool for SOH estimation has been extensively investigated in

the literature [16]. Another widely adopted technique for SOH estimation is incremental capacity analysis (ICA) and differential voltage analysis (DVA) [17]. Both methods have proven to be effective for aging diagnostics; however, their accuracy is strongly dependent on the applied current rate. In particular, lower current levels lead to more precise results, which may represent a significant limitation for EV applications.

- **Data driven approaches:** these approaches do not consider the physical laws of the battery systems as it is based on data-driven tools. Although these black-box approaches can provide good estimation accuracy, they require a large amount of data and high computational load.
- **Model based approaches:** models are used to reproduce the dynamic behavior of a battery: voltage response as a function of the input current, temperature and SOC. These approaches exhibit low complexity, low computational requirement and good estimation accuracy [18].

1.4. Principles of Electrochemical Impedance Spectroscopy

Electrochemical impedance spectroscopy is a widely adopted diagnostic tool for estimating battery degradation and SOH, as discussed in Section 1.3. EIS enables the measurement of the internal impedance of a battery over a wide frequency range. Two different types of EIS tests can be performed depending on the specific study objective, both leading to the same final outcome in terms of impedance characterization: galvanostatic electrochemical impedance spectroscopy (GEIS) and potentiostatic electrochemical impedance spectroscopy (PEIS). In the former, a small-amplitude sinusoidal current excitation at a given frequency is applied, while in the latter, a sinusoidal voltage excitation is imposed instead. Considering the GEIS case, during the test a sinusoidal current I_t at a given frequency is applied to the cell, and the resulting voltage response E_t is measured. The amplitude of this current is typically on the order of a few hundred milliamperes depending on the battery type (Equation 1.5). The measured voltage depends on the cell impedance; in particular, the phase shift ϕ in Equation 1.6 represents the voltage phase delay induced by the electrochemical impedance of the battery. In sinusoidal conditions, voltage and current can be represented by phasors (Equation 1.7). The impedance is then calculated

as the ratio between the voltage and current amplitudes, as expressed in Equation1.8.

$$I_t = I_0 sin(wt); w = 2\pi f \tag{1.5}$$

$$E_t = E_0 sin(wt + \phi) \tag{1.6}$$

$$\begin{aligned} \tilde{E} &= E_0 e^{j\phi} \\ \tilde{I} &= I_0 \end{aligned} \tag{1.7}$$

$$Z(w) = \frac{\tilde{E}}{\tilde{I}} = \frac{E_0}{I_0} e^{j\phi} = |Z| e^{j\phi} \tag{1.8}$$

The excitation frequency is swept over a wide range, e.g., from 10 kHz down to 10 mHz, in order to evaluate the impedance response of the battery at a range of frequencies, commonly known as frequency sweep. The battery is typically represented by an equivalent circuit model (ECM), where each circuit element describes the impedance behavior associated with different regions of the frequency spectrum. The high-frequency behavior is represented by an ideal inductor L and an ohmic resistance R. Subsequently, several RC branches are connected in series to represent the various electrochemical processes occurring within the cell. Many authors have adopted modeling approaches based on Zarc and Warburg elements, which provide a more accurate and realistic representation of the impedance response. A Zarc element consists of a parallel connection of a resistor R and a constant phase element (CPE). The impedance of a CPE is defined as:

$$Z_{CPE} = \frac{1}{(jw)^{\psi}\theta} \tag{1.9}$$

where θ is a general capacity and ψ is the depression factor. When the CPE is connected in parallel with a resistor, the resulting impedance defines the Zarc element:

$$Z_{arc} = \frac{1}{1/R + (jw)^{\psi}\theta} \tag{1.10}$$

ψ value ranges between 0 and 1, is responsible for the depression of the semicircle observed in Figure 1.5. For $\psi = 0$ Zarc reduces to a purely ohmic resistance, otherwise for $\psi = 1$ it corresponds to the ideal semicircle of a classical RC element. The Warburg element is defined by:

$$Z_w = R\frac{tanh(\sqrt{jw\theta})}{\sqrt{jw\theta}} \tag{1.11}$$

and shows a linear slope with an angle of 45° at high requencies. This linear slope describes the diffusion processes inside the cell. A simple way to approximate the Warburg element

is a series connection of resistor and a RC-element. [19] uses the following approximation for the Warburg element:

$$Z_w = R_1 + \frac{1}{1/R_2 + jwC_2} \tag{1.12}$$

for the estimation of parameters R_1, R_2 and C_2 it is required the frequency at which the spectrum reaches its minimum value [20].

The aforementioned features are illustrated in the Nyquist plot in Figure 1.6 which can be divided in three main sections. The high frequency region($\geq 1kHz$), or below 'x' axis region, is correlated to the to ionic conduction through the electrolyte and separator. The mid-frequency region represented by a semi-circle (approximately from $\leq 1kHz$ down to $\geq 100mHz$) is associated with charge transfer processes and the electrochemical double-layer capacitance. Depending on the aging state of the cell, a second semi-circle may appear at very high frequency, which is commonly attributed to the presence and growth of the SEI. Finally, the low-frequency region ($\leq 100mHz$), characterized by a slope of 45°, is attributed to the Warburg impedance and reflects diffusion-controlled phenomena [21]. In conclusion, EIS provides a clear representation of the evolution of the internal impedance, which depends on the behavior of the electrochemical processes occurring within the cell. This tool enables the monitoring of the battery SOH by highlighting changes in the internal resistance, which tends to increase with continued usage, thereby progressively hindering the flow of the required current.

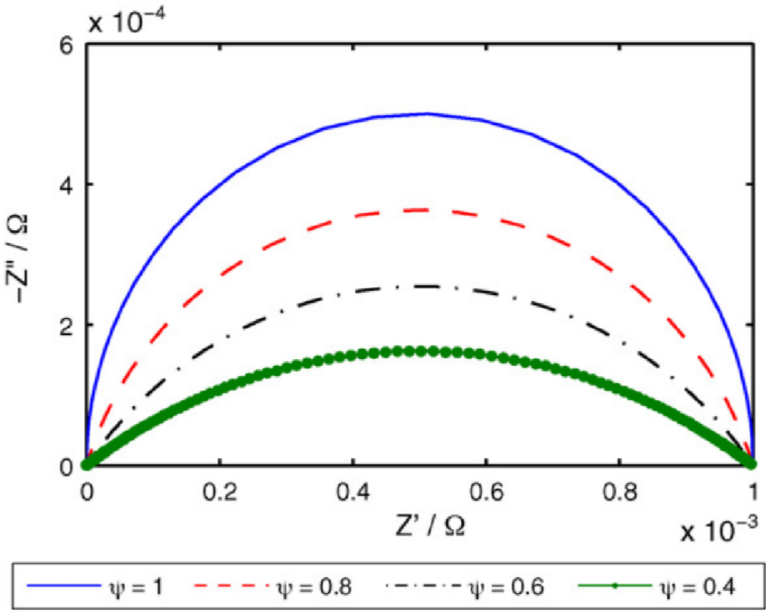

Figure 1.5: Impact of depression factor on the Nyquist plot of the Zarc element (R =1mΩ, C = 1 kF) [20].

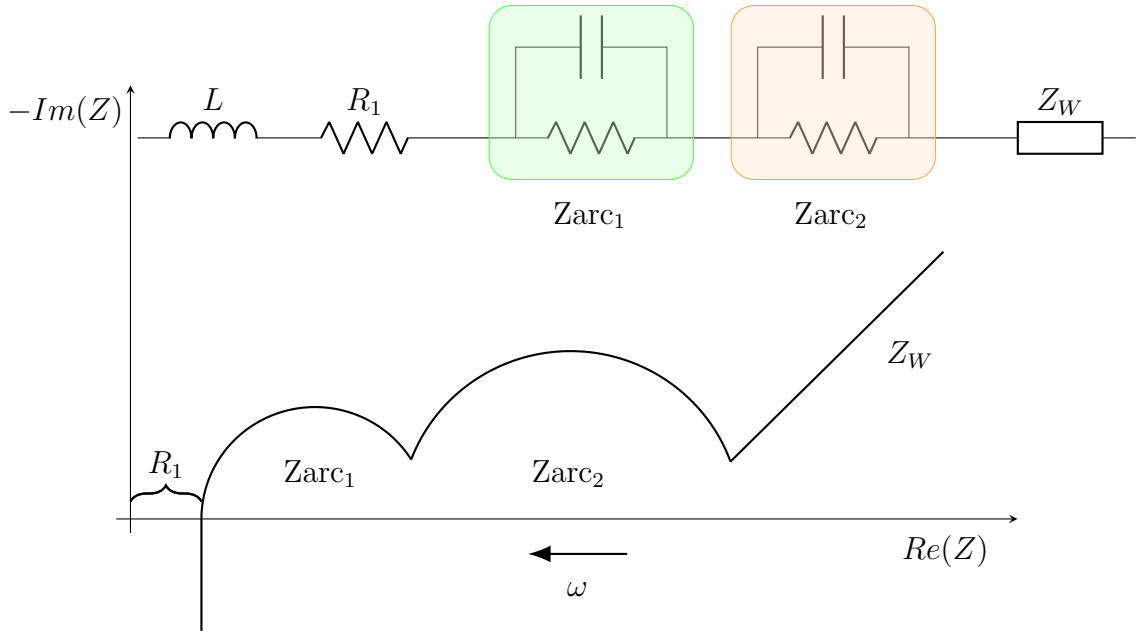

Figure 1.6: Ideal impedance spectrum of a LIB and an ECM with Zarc and Warburg element.

1.5. Challenges in online impedance estimation for EVs

In EVs applications, the use of EIS as a diagnostic tool is highly developed. Numerous researchers have proposed different methods for estimating the impedance spectrum online, in real time, with the aim of replacing conventional offline measurement techniques. These methods are referred to as offline because, in the context of an electric vehicle, measurements require the vehicle to be switched off and the battery to reach an electrochemical equilibrium state. This widely adopted approach, which is based on the technique described in Section 1.4, is extremely time-consuming. For this reason, companies such as Tesla, Ford, and General Motors have implemented on-board diagnostic solutions that combine impedance-based sensing with machine-learning-based voltage and current analytics for continuous monitoring of battery health throughout the EV lifetime [22]. However, implementing online EIS testing in an existing battery system remains highly challenging. This is mainly due to the need for dedicated hardware, which is often impractical, as well as the complexity associated with updating embedded firmware to enable switching-based perturbations for impedance measurement and state estimation. Conventional EIS measurements are inherently complex and slow processes, as the battery requires a long settling time to reach electrochemical equilibrium. This characteristic makes these techniques unsuitable for real-time applications. For these reasons, obtaining an impedance spectrum online

that can be implemented on-board automotive battery systems remains a significant technical challenge. One of the most critical limitations is the incompatibility between conventional measurement methods and the highly dynamic operating conditions of EVs. A second major limitation is the lack of controllable input signals. While such signals can be easily imposed in laboratory environments, in EV applications the battery current is dictated by driving conditions or charging events. Furthermore, battery impedance is strongly dependent on operating conditions. The parameters that most significantly affect impedance are temperature, SOC, and current. During real-time EV operation, these variables continuously change, leading to variations in impedance parameters and resulting in reduced measurement accuracy and degraded estimation performance. The study reported in [23] compares the impedance behavior at different temperatures for charged (non-blocking) and discharged (blocking) lithium-ion cells. The high-frequency semicircle exhibited similar behavior in both cell types across all temperatures, with a slight increase as temperature decreased. In contrast, the low-frequency semicircle increased dramatically with decreasing temperature. These results demonstrate that at lower temperatures the separation of EIS features becomes clearer and easier to distinguish.

At present, research on online EIS can be broadly classified into two main approaches: measurement-based methods and data-driven methods [24]. The former relies on dedicated hardware to generate excitation signals and compute the impedance spectrum using Fourier transforms. For example, [25] employed a motor controller to generate excitation currents and calculated the EIS by applying Fourier transforms to both excitation signals and their corresponding responses. Data-driven methods, on the other hand, have emerged in recent years with the advancement of artificial intelligence techniques. These approaches employ machine learning models to directly predict the impedance spectrum. The literature reports the use of three main types of input data: charging data [26], discharging data [27], and voltage–current signals recorded during pulse periods [28]. Despite the validity of the aforementioned methods, several considerations highlight the complexity of these approaches. In the case of hardware-based solutions, the acquisition of response signals requires high-speed sensors to satisfy the Shannon sampling theorem, leading to increased costs and greater BMS complexity [29]. For data-driven approaches, obtaining high-precision and high-sampling-rate current and voltage data comparable to laboratory measurements is particularly difficult. As a result, online EIS acquisition based on pulse data remains challenging in real-world applications [28]. Consequently, online EIS acquisition continues to represent a significant technical challenge in vehicle-based application scenarios.

2 | Modeling and simulation of driving cycles

2.1. Selection of vehicle benchmarks

The EV market is continuously growing, and technologies are becoming increasingly advanced. Improvements in lithium-ion battery diagnostic methods can further foster the development and adoption of electric vehicles. The first step of this project consists in the selection of reference vehicles. Three vehicle categories were chosen, ranging from an high-performance mid-size sedan to a compact urban vehicle, thus allowing the proposed methodology to be evaluated under significantly different operating conditions. The selected vehicles are the Tesla Model 3 Long Range AWD, the Peugeot e-208 54 kWh, and the Dacia Spring Electric 65. Battery performance was evaluated using vehicle benchmarks, including standardized driving cycles and vehicle parameters. In Table 2.1 the battery chemistry, the nominal capacity, the pack configuration and the cell shape are reported [22]. Three different cell shapes are considered in this work, namely cylindrical, prismatic, and

Table 2.1: Main battery pack characteristics of the selected electric vehicle benchmarks

Parameter	**Tesla Model 3 Long Range AWD**	**Peugeot e-208 (54 kWh)**	**Dacia Spring Electric 65**
Battery chemistry	NMC	NMC	LFP
Nominal capacity	82 kWh	54 kWh	26.8 kWh
Pack configuration	96s × 46p	102s × 1p	72s × 1p
Cell shape	Cylindrical (2170)	Pouch	Prismatic

pouch cells. Cylindrical cells consist of alternating layers of cathode and anode materials that are wound into a cylindrical shape. This structure makes cylindrical cells relatively easy and cost-effective from a manufacturing and maintenance perspective. Moreover, they exhibit high mechanical integrity, which makes them particularly robust when compared to prismatic and pouch cells. However, with regard to thermal behavior, cylindrical cells are

more sensitive to temperature gradients than the other two formats, as highlighted in [30]. Prismatic cells, on the other hand, are composed of stacked electrode layers arranged in foils and enclosed within a rigid casing made of aluminum or steel. This type of cell typically offers higher energy density but lower charge and discharge power capability compared to cylindrical cells. In addition, prismatic cells are generally larger in size; therefore, fewer cells are required to achieve the same overall energy content. Lastly, pouch cells differ from the other form factors mainly due to their non-rigid casing. They consist of flexible electrolyte layers enclosed in laminated films, typically made of plastic and aluminum, which results in a lower overall weight compared to cylindrical and prismatic cells. From a mechanical standpoint, the absence of a rigid casing leads to reduced structural strength. Furthermore, thermal management for pouch cells is particularly challenging, as these cells are prone to swelling caused by gas generation during operation. This phenomenon can be critical, since the resulting internal pressure may lead to deformation or failure of the battery enclosure.

The cell represents the fundamental building block in the hierarchical structure of a battery system. Each cell is characterized by a specific capacity and defined voltage limits. In real-world applications, especially in large-scale systems such as EVs, individual cells are not able to provide the energy required for proper operation. For this reason, multiple cells are electrically connected in series and in parallel. Series connections allow the overall voltage to be increased, whereas parallel connections increase the total capacity of the system. The battery module represents an assembly of cells electrically connected in series and in parallel. The notation XsYp indicates that X cells are connected in series and Y cells are connected in parallel. Finally, the last hierarchical level is the battery pack, which integrates battery cells, battery modules, the BMS, as well as cooling and protection systems. The design of an efficient battery pack requires a careful matching between technical specifications and the requirements imposed by the specific application. In the case of EVs, battery packs must withstand mechanical vibrations, impact forces, and temperature variations, while maintaining solid and stable structural integrity throughout the entire vehicle lifetime.

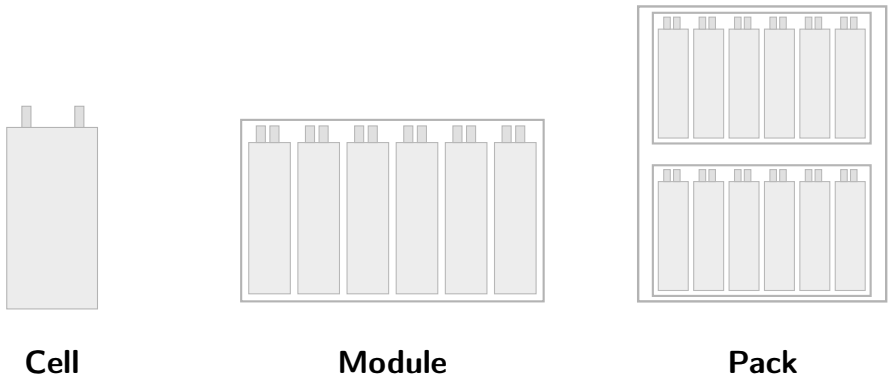

Figure 2.1: Hierarchical structure of an EV battery system: cell, module, and pack.

2.2. WLTP power profile generation and scaling

The worldwide harmonised light vehicles test procedure (WLTP) is a global standard used to assess vehicle emissions and environmental impact, and it is also used to determine the driving range of EVs. The WLTP cycle provides a standardized highly dynamic driving profile, making it suitable for reproducing realistic operating conditions. The WLTP framework includes several driving cycles known as the worldwide harmonised light vehicle test cycles (WLTC). These cycles are divided into three different classes, each of which is associated with a specific vehicle category [31]. The classification of vehicles is based on a parameter known as the power-to-mass ratio (PMR), defined as the ratio between the rated power of the vehicle (W) and its curb mass (kg), excluding the mass of the driver. In the case of WLTC Class 3 vehicles, a further subdivision is introduced based on the maximum vehicle speed (km/h). The above-mentioned aspects are summarized in Table 2.2. The WLTC driving cycles were used to derive the time-dependent power profiles of the three selected vehicles. In [22], the characteristics of each vehicle are reported; in this case, the parameters relevant for assigning the vehicles to the corresponding WLTC classes were selected. The Tesla and Peugeot vehicles belong to the Class 3b vehicles while Dacia is considered a Class 3a vehicle.

Table 2.2: WLTC test cycles classifications

WLTC Class	PMR [W/kg]	v_{max} [km/h]
Class 1	PMR $\leq$ 22	-
Class 2	22 $<$ PMR $\leq$ 34	-
Class 3a	PMR $>$ 34	$<$ 120
Class 3b	PMR $>$ 34	$\geq$ 120

The velocity profiles are generated using the MATLAB-based driving cycle library (drivingcycle v2.1.8) which provides standardized speed-time profiles for the different classes. In Figure 2.2, the target velocity profile for a Class 3 vehicle is shown. The difference between the two subclasses lies in the maximum speed limit of 120 km/h, as already highlighted in Table 2.2. When a Class 3a vehicle reaches its maximum achievable speed, it is no longer able to follow the target profile in the highest-speed segment, also referred to as the extra-high phase. In this last section, the target profile reaches a maximum speed value of 131.3 km/h.

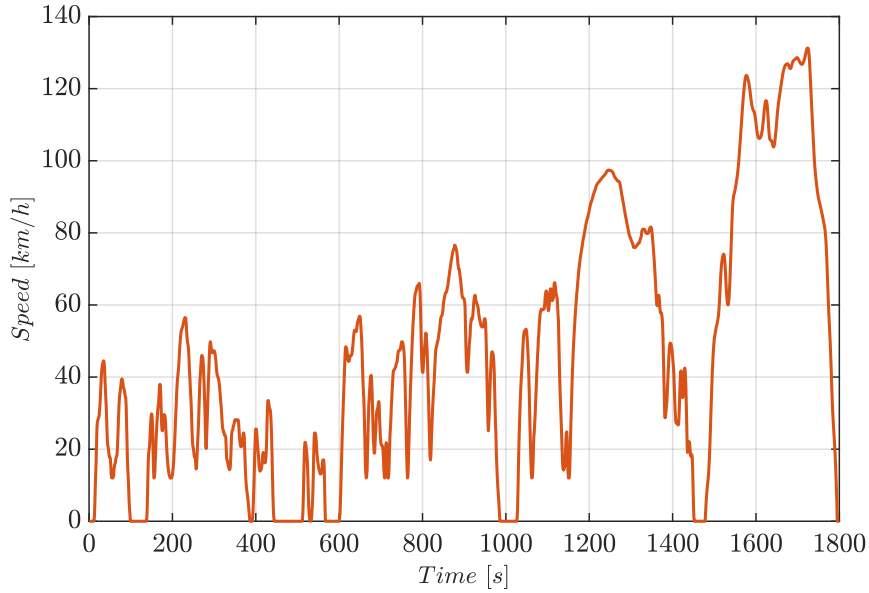

Figure 2.2: Standard speed-time WLTP profiles for Class 3 vehicles.

A longitudinal vehicle dynamics model was adopted to compute the traction power required during the driving cycle. Starting from these data the power profiles are obtained

using the following formula for each vehicle as represented in Figure 2.3:

$$P(t) = F_{tot}(t)v(t) \tag{2.1}$$

where F_{tot}(t) represents the total longitudinal force acting on the vehicle. This force is obtained as the sum of several contributions:

$$F_{tot}(t) = F_{acc}(t) + F_{aero}(t) + F_{roll}(t) + F_{grade}(t) \tag{2.2}$$

where:

- **acceleration force:** $\mathrm{F_{acc}(t) = m\frac{dv(t)}{dt}}$ required by the vehicle to accelerate or decelerate;
- **aerodynamic drag force:** $\mathrm{F_{aero}(t) = \frac{1}{2}\rho C_d A v^2(t)}$ models the resistance of the air drag which significant at high speeds since it increases quadratically with the vehicle speed;
- **rolling resistance force:**$\mathrm{F_{roll}(t) = mgC_r}$ it accounts for energy losses due to the contact with the road surface;
- **grade resistance force**: $\mathrm{F_{grade}(t) = mgsin(\theta)}$ associated with road slope. In WLTP-based simulations the road grade is assumed to be zero so this term will not be considered in the calculations.

Considering the aforementioned aspects the final form of the power-time profile is the following:

$$P(t) = v(t)[m\frac{dv}{dt} + \frac{1}{2}\rho C_d A v^2(t) + mgC_r] \tag{2.3}$$

The dimensionless coefficients $\mathrm{C_d}$ and $\mathrm{C_r}$ represent the aerodynamic drag coefficient and the rolling resistance coefficient, respectively. The former describes the aerodynamic efficiency of the vehicle, while the latter accounts for the energy losses associated with tire–road contact. Modern passenger vehicles typically exhibit $\mathrm{C_d}$ values between 0.25 and 0.33. Highly streamlined EVs, such as the Tesla Model 3, can achieve even lower values, with $\mathrm{C_d} = 0.23$. In contrast, more compact vehicles with less aerodynamically optimized designs are characterized by higher values; accordingly, values of 0.29 and 0.33 were selected for Peugeot and Dacia vehicles, respectively. Regarding $\mathrm{C_r}$, a constant value of 0.010 was adopted for all three cases, which is consistent with typical values reported in the literature for passenger car tires operating on paved road surfaces [32].The term A represents the vehicle frontal area, defined as the portion of the vehicle that is directly

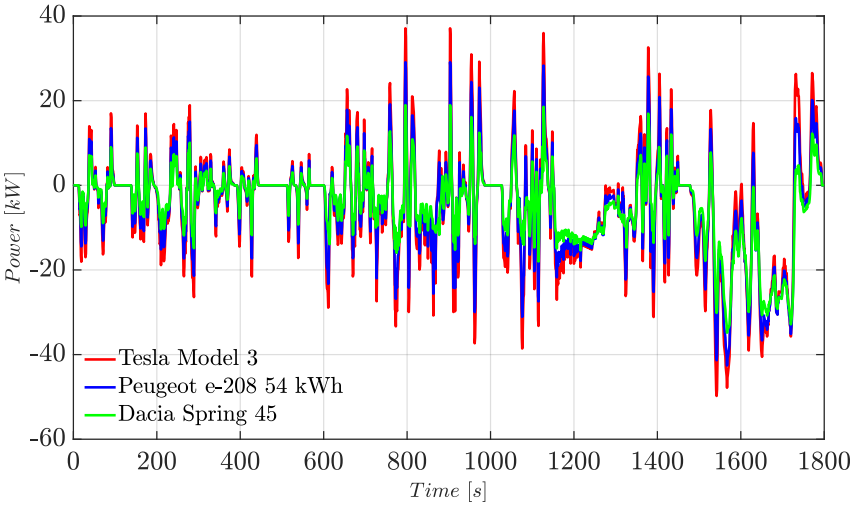

Figure 2.3: Power profiles from the WLTP driving cycles.

exposed to the oncoming airflow. In Table 2.3 the main parameters chosen for each vehicle are summarized. The power profiles were initially scaled from vehicle-level power

Table 2.3: Main vehicle parameters

Vehicle model	Mass (kg)	Frontal Area (m^2)	C_d (-)	C_r (-)	Power (kW)
Tesla Model 3	1919	2.66	0.23	0.010	366
Peugeot e-208	1530	2.50	0.29	0.010	115
Dacia Spring	1032	2.46	0.33	0.012	48

to battery-level power for each selected vehicle. Subsequently, in order to perform the experimental tests under laboratory conditions, an additional scaling step was required to adapt the profiles to the battery cells available for testing. A scaling factor K was introduced and defined as the ratio between the battery energy of the actual vehicle pack and the energy of the laboratory test cells. This factor was used to appropriately scale the battery power profiles, ensuring consistency between vehicle-level operating conditions and cell-level experimental constraints. The scaled battery power profiles (Figure 2.4) derived in this chapter are subsequently used as input for the experimental tests described in Chapter 3.

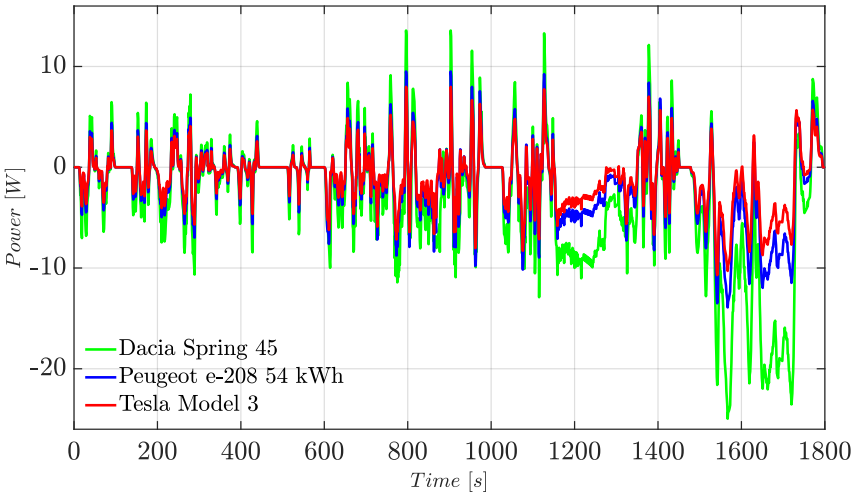

Figure 2.4: Cell-level scaled power profiles.

3 | Experimental setup and methodology

3.1. Laboratory test bench configuration

The experimental activities were carried out at the PeDS laboratory of Politecnico di Milano, where battery testing and analysis were performed using the BTLab software environment. Two different lithium-ion cell chemistries were considered in this work in order to evaluate the proposed methodology under diverse electrochemical characteristics. The selection of the cells was driven by the actual chemistries used in the lithium-ion batteries of the selected vehicles. Accordingly, two NMC cells were used for the Tesla and Peugeot power profiles, whereas an LFP cell was employed for the Dacia case. The NMC cells are Samsung INR21700-50E/21700, with a nominal capacity of 4.9 Ah, while the LFP chemistry is represented by IFR32650/32700 cells with a nominal capacity of 6.5 Ah. All tests were conducted on single-cell configurations directly connected to the test equipment. A BioLogic battery cycler was employed to apply controlled charge and discharge profiles to the cells under test. The cycler supported different control modes, including constant-current and power-controlled operation, enabling flexible reproduction of realistic operating conditions. The battery cycler was interfaced with a control PC via the BTLab software, which provided real-time monitoring of voltage and current signals as well as continuous data acquisition for post-processing and analysis. Voltage and current measurements were supplied by the internal sensors of the cycler, while temperature was monitored to ensure safe operation throughout the experimental campaign. All experiments were conducted under ambient laboratory temperature conditions. Figure 3.1 illustrates the laboratory setup used for the experimental analysis of the cells. Through the BTLab software installed on the laboratory PC, it is possible to design and execute specific test programs according to the intended analysis. The battery cycler then follows the commands defined in these programs and, via the connecting cables, interfaces directly with the batteries under test. Figure 3.1 (b) shows the test bench where the cells used in the experiments are placed. Two cables are connected to the terminals of each cell:

the thicker cable is used to supply or draw current, while the thinner one is dedicated to measurement. The red and black cables connected to the cell electrodes represent the positive and negative polarities, respectively. Lastly, the thin green cable, also connected to the battery cycler, is used to monitor the temperature evolution during the experimental tests.

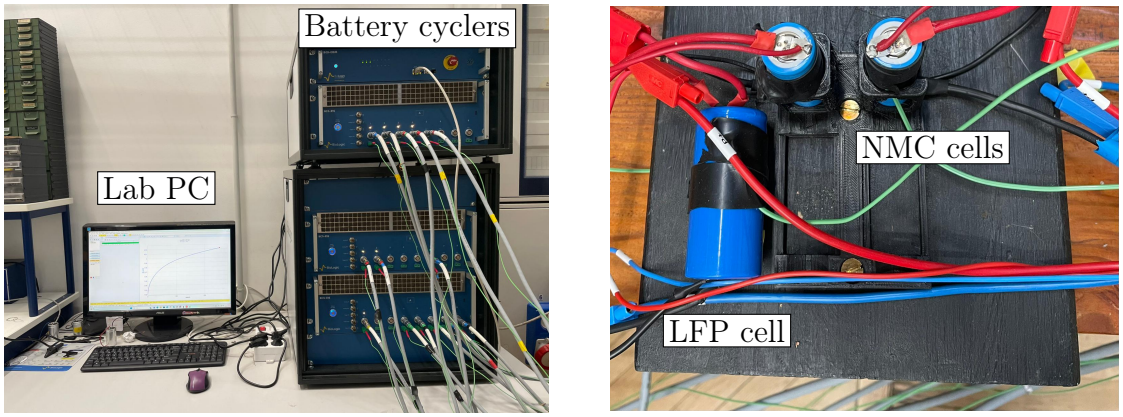

(a) (b)

Figure 3.1: Laboratory experimental setup: (a) control workstation and Biologic battery cyclers; (b) test bench hosting the three battery cells used in the experimental analysis.

3.2. Experimental test protocol

Preliminary charge–discharge cycles were performed on the cells under investigation before proceeding with more advanced experimental tests. This initial activation phase was performed through a few charge–discharge cycles at a controlled C-rate in order to bring the cells to a stable and repeatable operating condition before the experimental campaign. In practice, early cycles allow the cell response to settle and reduce transient effects that may occur in freshly handled cells, such as drifts in terminal voltage and apparent capacity. Moreover, the activation cycling provides a reliable baseline in terms of capacity and internal resistance, ensuring that the subsequent EIS measurements and dynamic tests are representative of the cell behavior under nominal operating conditions. Six constant-current (CC) charge and discharge cycles were performed for each cell and an upper cutoff voltage limit and a lower cutoff voltage limit were applied respectively (Figure 3.2). The operating voltage range for these first cycles of the NMC cells is 2.7–4.15 V, while the LFP cells operate within a voltage range of 2.3–3.5 V. Following the initial capacity test, additional experiments were conducted using the GEIS technique implemented in the BTLab software. The corresponding experimental setup for the NMC cell is shown in Figure 3.3, in the case of the LFP cell the only variable changed is the amplitude I_a. The

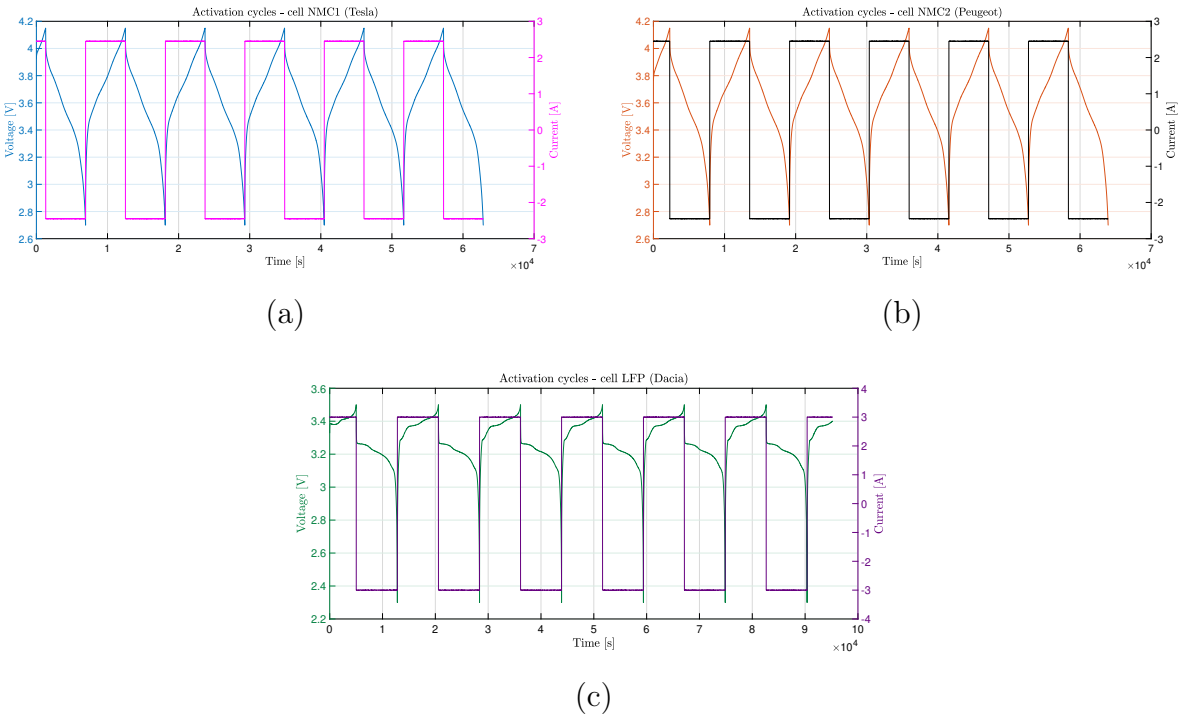

Figure 3.2: Voltage vs time profiles for the three cells: (a) NMC 1; (b) NMC 2; (c) LFP.

application of this technique is based on the principle that the controlled variable is a sinusoidal current, from which the resulting impedance is evaluated. The amplitude of the current sine signal, denoted as I_a, was selected after performing several preliminary tests on the cells. For the NMC cells, a current amplitude of 100 mA was identified as providing the least distorted response, whereas for the LFP cells a higher value of 200 mA was selected. The parameter N_d represents the number of points per decade, N_a while denotes the number of measurements performed at each frequency, whose average value is returned. Finally, the frequency range limits are defined by the value of f_i (upper frequency limit) and f_f (lower frequency limit).

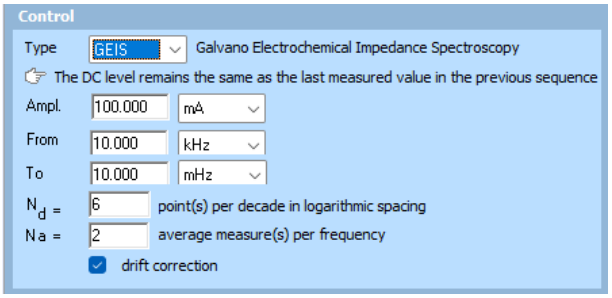

Figure 3.3: GEIS experimental setup for the NMC cell implemented in the BTLab software environment.

Subsequently, a stepped constant-current discharge test was performed, consisting of 10% state-of-charge decrements starting from 100%. The process is repeated also in the recharging phase. At each step, an EIS measurement was carried out, in order to obtain information on the impedance at each variation of the state of charge. Figure 3.4 shows the state-of-charge evolution of all three cells, it is evident the differences observed between the two chemistries. In the case of both NMC cells, during the recharge phase it was not possible to reach 100% SOC, as the process stopped at approximately 80%. On the other hand, the LFP cell, subjected to the same test, completed the recharge phase up to 100% SOC. this aspect will be deeply investigated in Chapter 5. EIS measurements carried out at different state-of-charge levels were essential for validating the wavelet transform methodology for the online estimation.

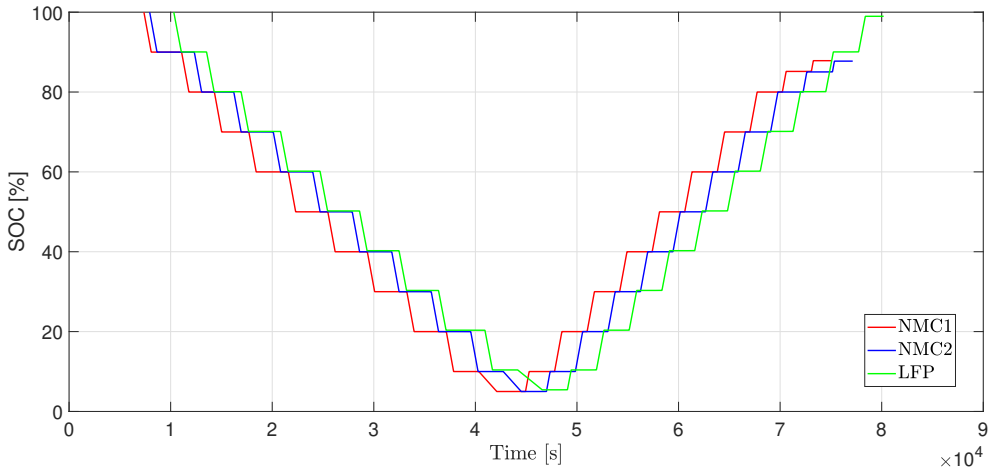

Figure 3.4: SOC evolution of the three cells during the stepped discharge–charge test.

The driving range of the three vehicles was obtained by fully discharging the three cells starting from 100% SOC, using the previously derived power profiles. Using the LOOP function in BTLab, these cycles were repeated until the minimum voltage limit was reached. Each cell reached its lower voltage limit after a different number of cycles, due to the substantial differences in the power profiles derived from the characteristics of the individual vehicles. Specifically, the Tesla, Peugeot, and Dacia driving cycles were repeated 32, 22, and 13 times (N), respectively, before the cell was fully discharged. To compute the total driving range, the distance covered during a single 1800 s cycle was first calculated according to the following formula:

$$s_{WLTC} = \int_{t_0}^{t_f} v(t)\, dt \tag{3.1}$$

where t_0 is equal to 0 seconds, while t_f is the standard duration of the cycle equal to 1800 seconds. Subsequently, in order to compute the total distance traveled and thus the driving range, a corrective factor was introduced to account for the fact that the final cycle was not completed but was interrupted before the nominal duration of 1800 s due to the attainment of the voltage cutoff limit. The total distance covered up to the last complete WLTC cycle of 1800 s was first calculated multiplying the distance of one cycle by the number of loops completed $\mathrm{N}-1$ (Equation 3.2). Then, the space traveled during the final cycle, characterized by a duration shorter than 1800 s (Equation 3.3), was evaluated. By summing these two contributions, the final driving range was obtained (Equation 3.4).

$$s_{N-1} = s_{WLTC} \cdot (N-1) \tag{3.2}$$

$$s_{last} = \int_{t_0}^{t_f} v(t)\, dt \tag{3.3}$$

$$s_{tot} = s_{N-1} + s_{last} \tag{3.4}$$

In order to validate the online EIS estimation method based on the wavelet transform, the following experimental test was finally carried out. The cell was first charged using a CC–CV protocol and subsequently left to rest for 45 minutes in order to allow the battery to reach conditions closer to electrochemical equilibrium. After the rest period, an EIS measurement was performed. Subsequently, a WLTC driving cycle with a duration of 1800 s was applied using the urban profile (UP) technique implemented in the BTLab software environment. Specifically, the voltage and current signals of the profile were acquired with a temporal resolution of 2 ms, corresponding to a sampling frequency of 500 Hz. This choice was motivated by the fact that wavelet-based analysis allows frequency information to be extracted up to 250 Hz, in accordance with the Nyquist-Shannon sampling theorem [33]. A rest period of 1 s was introduced with the purpose of separating the WLTC cycle from the subsequent impedance measurement. The steps described above were repeated for the following SOC levels: 100%, 75%, 50%, 25%, 5%. This experimental protocol enables the application of EIS measurements to realistic dynamic profiles such as the WLTC and allows the comparison and validation of the final results obtained through wavelet-based impedance estimation.

3.3. Methodology of Differential Voltage Analysis

Differential voltage analysis is a conventional method used to investigate capacity loss and aging mechanisms in lithium-ion batteries. The main feature of this method is

that it allows voltage plateaus to be transformed into peaks in the dV/dQ curves. These peaks describe the phase transition characteristics of the cell during the intercalation and deintercalation processes of lithium ions in the active material. Through monitoring the location, magnitude, width and area of these peaks, it is possible to study how the cell electrohemistry changes over the lifetime of a battery and to estimate its SOH [34]. DVA generally provides highly accurate results when applied at very low constant current rates. Nevertheless, [35] employes this tool at higher C-rates to investigate calendar aging in an LFP cell, with particular focus on the inhomogeneous lithium distribution within the anode, which is correlated with the observed DVA peaks. Similarly, [36] demonstrates that the shape of these curves may shift or even generate additional peaks when higher C-rates are used. The application of polarization compensation is shown to reduce the effect of resistive voltage drops, enabling the extraction of quasi-OCV curves. This approach facilitates the identification of electrochemical peaks associated with phase-equilibrium transitions within the cell. Furthermore, [37] applies DVA to analyze the shift of such curves by distinguishing between charge and discharge phases and by comparing the behavior of a fresh cell with that of an aged cell subjected to cycling degradation.

From a mathematical standpoint, the DV curve is obtained as the gradient of the voltage V with respect to the capacity Q using the following equation:

$$\frac{dV}{dQ} \approx \frac{\Delta V}{\Delta Q} \tag{3.5}$$

In the analysis carried out in this work, the DV curve is evaluated as dV/dSOC rather than as a function of the capacity. By definition, the SOC is the ratio between the actual capacity and the nominal capacity of the cell. The derivative with respect to SOC can be readily obtained by multiplying dV/dQ by the nominal capacity of the cell (Equation 3.6) [38]. In this way, the results are normalized with respect to the nominal capacity, allowing an easier comparison between cells with different capacities.

$$\begin{aligned} SOC &= \frac{Q}{Q_{\text{nom}}} \\ \frac{\mathrm{d}V}{\mathrm{d}SOC} &= \frac{\mathrm{d}V}{\mathrm{d}Q} \cdot \frac{\mathrm{d}Q}{\mathrm{d}SOC} = Q_{\text{nom}} \cdot \frac{\mathrm{d}V}{\mathrm{d}Q} \end{aligned} \tag{3.6}$$

Moreover DVA represents a topic of significant interest within the research community. [38] proposes a general framework for capacity correction and SOC estimation by extracting three main features from DV profiles of LIBs. The present work instead aims to find peaks of the DV curve in LFP cells specifically, after applying the derivative with respect to SOC over a real driving profile. This derivative is very challenging to compute, since the strong

signal dynamics make the identification of even a single peak particularly challenging. In Figure 3.5 are represented the voltage trend for the two most used chemistries in the automotive sector. By comparing the curves, it is possible to observe that the NMC cell exhibits a significantly steeper slope compared to the LFP cell. In the first case, the derivative $dV/dSOC$ remains non-zero over almost the entire operating range, and each voltage value corresponds to a unique SOC. This aspect makes the $OCV(SOC)$ relationship mathematically invertible, allowing SOC estimation through direct inversion of the voltage–SOC function without relying on derivative-based methods. In contrast, LFP cells exhibit an extended voltage plateau where $dV/dSOC$ is very small. As a result, voltage changes only marginally with SOC, and even minor measurement errors can lead to significant SOC estimation inaccuracies. Under these conditions, OCV-based estimation alone is insufficient, thereby motivating the use of more advanced techniques such as DVA.

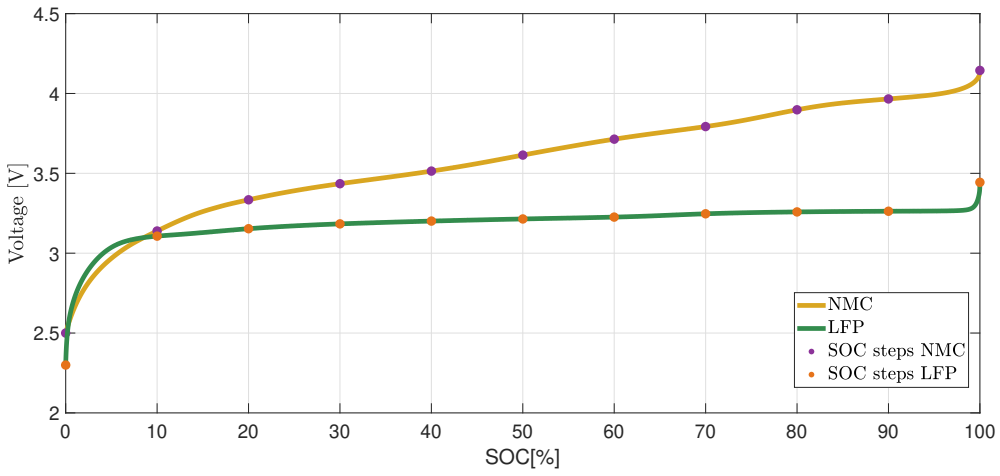

Figure 3.5: Discharge curves of NMC and LFP cells.

The reference curve used for the estimation of the peaks is the dOCV/dSOC profile. Indeed, this trend describes the state of the electrodes after the relaxation of kinetic processes, thereby providing relevant information from a thermodynamic standpoint. Accordingly, dOCV/dSOC curve exhibits the so-called "true" peaks, corresponding to the exact moments at which electrochemical processes occur within the cell. These peaks map the actual SOC of the battery.

Two different methodologies were investigated to track peaks in the DV curve obtained from the WLTP profile repeated until complete cell discharge. The LFP cell used for the tests has the same specifications as the one described in Chapter 3. The initial step in

both approaches consists of obtaining the $OCV(SOC)$ curve. It is derived by interpolating the corresponding resting voltage value at each SOC step using the data from the 10% SOC stepped CC discharge/charge test described in the last part of the previous section. The SOC is computed using the Coulomb counting formula:

$$SOC(t) = SOC(t_0) - \frac{1}{Q_{nom}} \int_{t_0}^{t} I(\tau)\, d\tau \tag{3.7}$$

Moreover, due to the dynamic behavior of the WLTP driving cycle, it is necessary to compensate for the voltage drop across the internal resistance of the battery. This correction step is crucial because the fast dynamics caused by the continuous changes in the sign of the current would otherwise lead to the appearance of "fictitious" peaks in the DV curve, which are not meaningful from a diagnostic perspective. At this stage, the two approaches employ different methodologies to obtain the DV curve from the WLTP profile and identify the corresponding electrochemical peak. In both cases, the detected peaks are consistent with each other and also with the reference peak derived from the $dOCV/dSOC$ curve. The two techniques and their respective results are described in detail in Chapter 5. The identification of a peak within a dynamic profile such as a real driving cycle represents a reference point for internal electrochemical processes occurring within the cell. Furthermore, monitoring these signatures in the DV profile forms the basis for studying the cell SOH. With aging, these peaks may shift and change amplitude, and their analysis enables the estimation of degradation, lithium loss, or structural changes within the cell.

4 | Wavelet-based online EIS estimation

4.1. Theoretical overview of Wavelet Transform in power signal analysis

A wave is defined as an oscillatory function of time or space, such as a sinusoidal waveform. A wavelet, also referred to as a *small wave*, is a localized oscillation that extends over a short time interval. The wavelet transform (WT) is a mathematical transformation applied to specific wavelets under predefined constraints. This tool is used to convert a signal from the time or space domain into the joint time–frequency or space–frequency domain, respectively. Prior to the development of WTs, signal analysis was primarily based on Fourier transforms (FTs), which are characterized by the conversion from the time or space domain to the frequency domain through the use of orthogonal sine and cosine functions. Anyway this tool has some limitations in the study of non stationary signals, as a consequence the wavelets became a main topic in the analysis of power signals. Wavelets still exhibit an oscillatory, wave-like behavior, but at the same time they enable the simultaneous analysis of time and frequency. A wavelet has its energy concentrated in time, which makes it a fundamental tool for the analysis of transient phenomena. In Figure 4.1, a sinusoidal oscillating wave with constant amplitude over the interval $-\infty \leq t \leq +\infty$ is illustrated; as a result, it possesses infinite energy in time. By contrast, the wavelet shown in the figure has finite energy localized around a specific point in time [39].

(a) (b)

Figure 4.1: (a): Sine wave; (b) Daubechies' Wavelet ψ_{D20}.

Unlike WTs, FTs are not capable of revealing the time support of frequency components, as it is showed in Figure 4.2. Both time-domain signals exhibit different frequency contents arranged in an inverted manner; nevertheless, their frequency-domain response is identical. This highlights a major limitation of the FT: it provides the frequency response in both cases, but it does not convey any information about when changes in the signal's frequency content occur over time. Such temporal information cannot be reconstructed from the spectrum alone. This represents a key drawback of FT-based analysis when dealing with non-stationary power signals. This limitation represents one of the main reasons for the widespread adoption of wavelet transforms in signal analysis. In principle, the application of a sliding window to the FT allows only specific portions of a signal in the time domain to be converted into the frequency domain, thereby enabling the identification of the time support of frequency components. This approach is implemented through the short-time Fourier transform (STFT) [40]. However, this method presents a fundamental drawback that must be considered: the use of a fixed window length, which is independent of the analyzed frequency. Narrow windows may lead to inaccurate analysis at low frequencies, since longer time intervals are required to complete a full oscillation. In contrast, excessively wide windows may capture multiple frequency components occurring within the same time interval, thus preventing an accurate localization of the signal content in time [41].

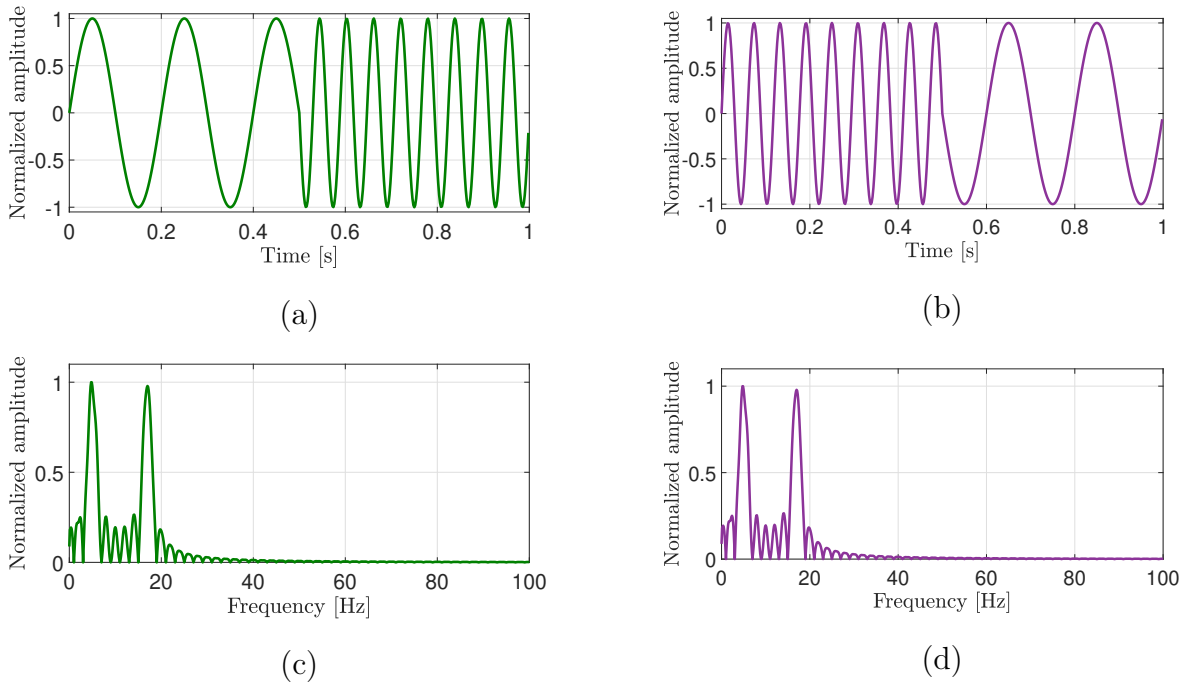

Figure 4.2: Time-domain signals (a) and (b) and corresponding magnitude Fourier transforms (c) and (d). In (a), a 5 Hz sinusoid precedes a 17 Hz sinusoid, while in (b) the order of the two components is reversed.

For the aforementioned reasons, wavelets provide a suitable alternative to sinusoidal basis functions and Fourier transform–based approaches. A function $\psi(\mathrm{x})$ is considered a wavelet if the following conditions are satisfied:

$$\int_{-\infty}^{+\infty} \psi(t)dt = 0 \tag{4.1}$$

$$\int_{-\infty}^{+\infty} \frac{|\hat{\psi}(w)|^2}{w} dw \equiv C_\psi < \infty \tag{4.2}$$

The condition 4.2 is fundamental to reconstruct a function from a decomposition into wavelets. The first wavelet, introduced in 1909, is the Haar wavelet defined by:

$$\psi(x) = \begin{cases} 1 & 0 \leq x < 1/2 \\ -1 & 1/2 \leq x < 1 \\ 0 & \text{otherwise} \end{cases}$$

it is very simple and helpful for the computation of wavelet transforms but since it is not continuous, it is not useful as other wavelets for analyzing continuous signals. Another

widely used wavelet family is the Daubechies-2p. These are wavelets with p vanishing moments to represent polynomials of degree at most p - 1. A Daubechies-2 wavelet is equivalent to the Haar wavelet. As p increases the number of scales required decreases while the support of the wavelet grows with p [42]. The most popular wavelet functions are shown in Figure 4.3.

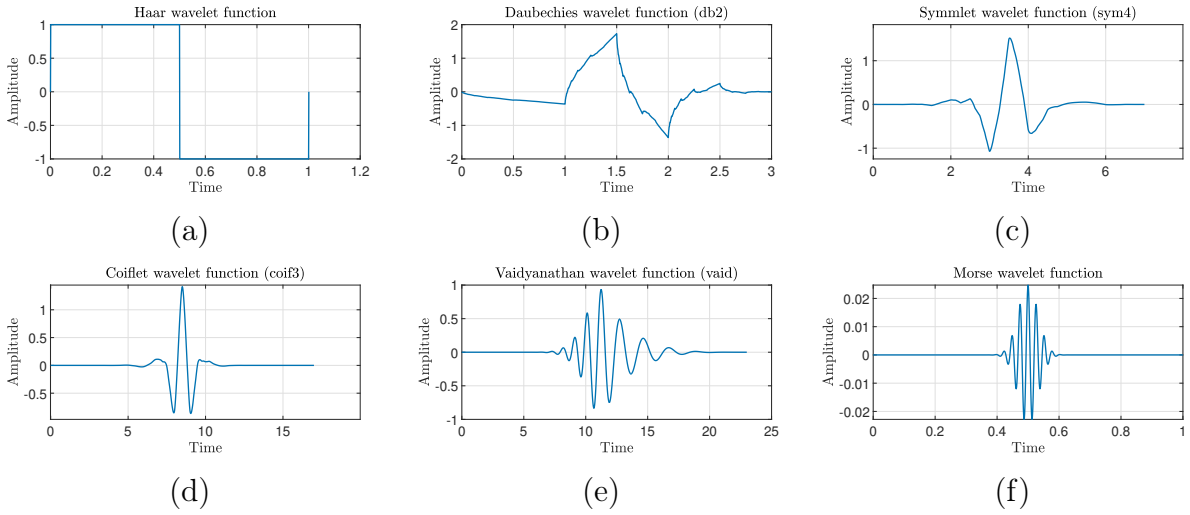

Figure 4.3: Wavelet functions: (a) Haar, (b) Daubechies, (c) Symmlet, (d) Coiflet, (e) Vaidyanathan, (f) Morse.

The core of wavelet analysis is the concept of *wavelet family*, which is defined as the set of functions obtained through the translation and dilation of a given wavelet. A wavelet family with *mother wavelet* ψ(t) consists of functions $\psi_{a,b}(t)$ of following form:

$$\psi_{a,b}(t) = \frac{1}{\sqrt{a}}\psi\left(\frac{t-b}{a}\right) \tag{4.3}$$

where b is the *shift* or *center* of $\psi_{a,b}$ and a is the *scale*. Alternatively, the scaling factor 1/a may be used. By shifting the wavelet function through the parameter b, the time-domain signal under analysis can be fully covered. Similarly, by dilating or compressing $\psi(t)$ as a function of the parameter a, it is possible to modify the width of the wavelet function, allowing the analysis of specific frequency components, behaving like a band-pass filter. If $a > 1$, $\psi_{a,b}$ is obtained by stretching the wavelet function $\psi(t)$, whereas if $a < 1$, the wavelet is compressed. The scale parameter a thus corresponds to the concept of frequency in Fourier analysis.

WTs can be divided into two main categories: continuous wavelet transforms (CWTs) and discrete wavelet transforms (DWTs). CWTs operate over all possible window lengths

and positions, providing a continuous representation of the signal in the time–scale domain. The CWT is defined by the following expression:

$$CWT(a,b) = \frac{1}{\sqrt{a}} \int_{-\infty}^{+\infty} x(t)\psi\left(\frac{t-b}{a}\right) dt \tag{4.4}$$

where $x(t)$ denotes the input signal under analysis and $1/\sqrt{a}$ represents a normalization factor [41]. $CWT(a,b)$ correlates the time-domain signal with a wavelet that is shifted and dilated according to the selected scale and translation parameters, as illustrated in Figure 4.4. Figure 4.4 (b) highlights the main characteristic of wavelet analysis, namely the ability to represent in time when changes in the frequency content of a signal occur. The side color bar represents the normalized wavelet power expressed in decibels: a value of 0 dB corresponds to the maximum intensity, while negative values indicate a reduction in intensity relative to the maximum. When the wavelet is far from a transition point, it captures only the frequency components of interest. In contrast, when it reaches the region where the signal undergoes a frequency change, it captures components at two different frequencies simultaneously, generating a cloud-like region around the transition point until the signal stabilizes at the new frequency.

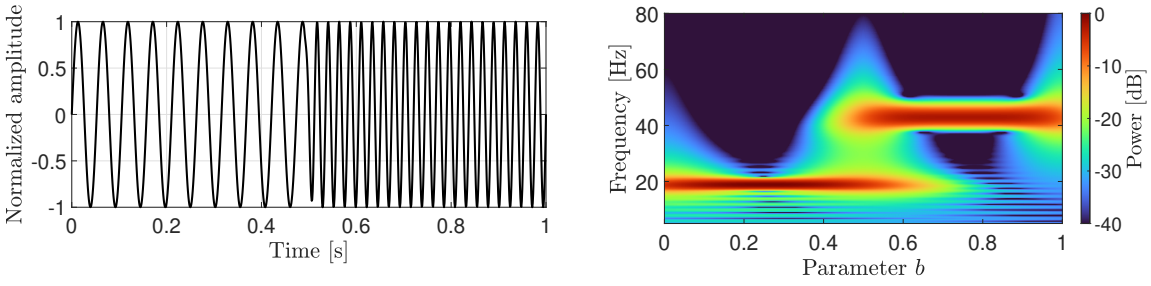

(a) (b)

Figure 4.4: (a): The signal x(t) where from 0 to 0.5 s and from 0.5 to 1 s the frequencies are 19 Hz and 43 Hz, respectively; (b): $CWT(a,b)$ plot where the vertical axis is the inverse of scale $(1/a)$ which, in practice, corresponds to the frequency.

In the case of DWTs, CWTs are adapted by modifying the scale parameter a so that the band-pass wavelet function is progressively scaled by a factor of 2, corresponding to a halving of the bandwidth. This discretization is effective over the entire frequency range except at 0 Hz, for which an infinite number of operations would be required. For this reason, in addition to the use of a band-pass filter, a low-pass filter is also required. This filter is represented by the scaling function $\phi(t)$, which corresponds to the orthogonal complement of the wavelet function $\psi(t)$ in the time domain. The scaling

function is also referred to as the *father wavelet* and, together with the mother wavelet, enables the representation of the time signal. The scale and translation parameters are chosen as $a = 2^{-j}$ and $b = k2^{-j}$ where j and k are integer numbers. These parameters represent the decomposition level, or refinement level, and the variable controlling the shifting, respectively [41]. The selection of these parameters is crucial for the accuracy of the analysis, since excessively large values may lead to the construction of a redundant orthogonal family, while excessively small values may result in an incomplete representation of the transformed signal [42]. Therefore, considering $\psi(t)$, substituting the parameters aforementioned a and b and assuming a normalization factor equal to $1/\sqrt{a}$, it is possible to derive the corresponding functions $\psi(t)$ and $\phi(t)$:

$$\psi\left(\frac{t-b}{a}\right) = \frac{1}{\sqrt{a}}\psi(2^{-j}t-k) = \frac{1}{\sqrt{2^{-j}}}\psi(2^{-j}t-k) = 2^{\frac{j}{2}}\psi(2^{-j}t-k) \tag{4.5}$$

$$\phi(t-b) = a\phi(t-k2^{-j}) = 2^{-j}\phi(2^{-j}t-k) \tag{4.6}$$

Nevertheless, although DWTs are formulated using selected values of a and b, it is applied to continuous signals in time. Since voltage and current measurements acquired in digital systems are inherently sampled, the discrete-time wavelet transform (DTWT) is adopted. DTWTs are based on filter-bank-based decomposition using two filters: a low-pass filter $h[\cdot]$ to capture low-frequency components and a high-pass filter $g[\cdot]$ characterized by a mirrored frequency response, extracting the high-frequency content. Unlike CWTs and DWTs, this methodology is based on a tree-structured filtering process, followed by downsampling operations. A widely used extension of this framework is the discrete-time wavelet packet transform (DTWPT), which allows a uniform and equally distributed time–frequency resolution over the full spectrum. This property enables a more flexible analysis across a broader frequency range, which is particularly advantageous when dealing with dynamic power profiles. In Figure 4.5 are illustrated the two aforementioned strategies. These discrete-time wavelet-based transforms are therefore particularly well suited for the analysis of current and voltage signals measured by the BMS at the battery pack level, and constitute a key enabler for online EIS under dynamic operating conditions. Anyway in this work the CWT will be used to extract impedance-based information from the signal.

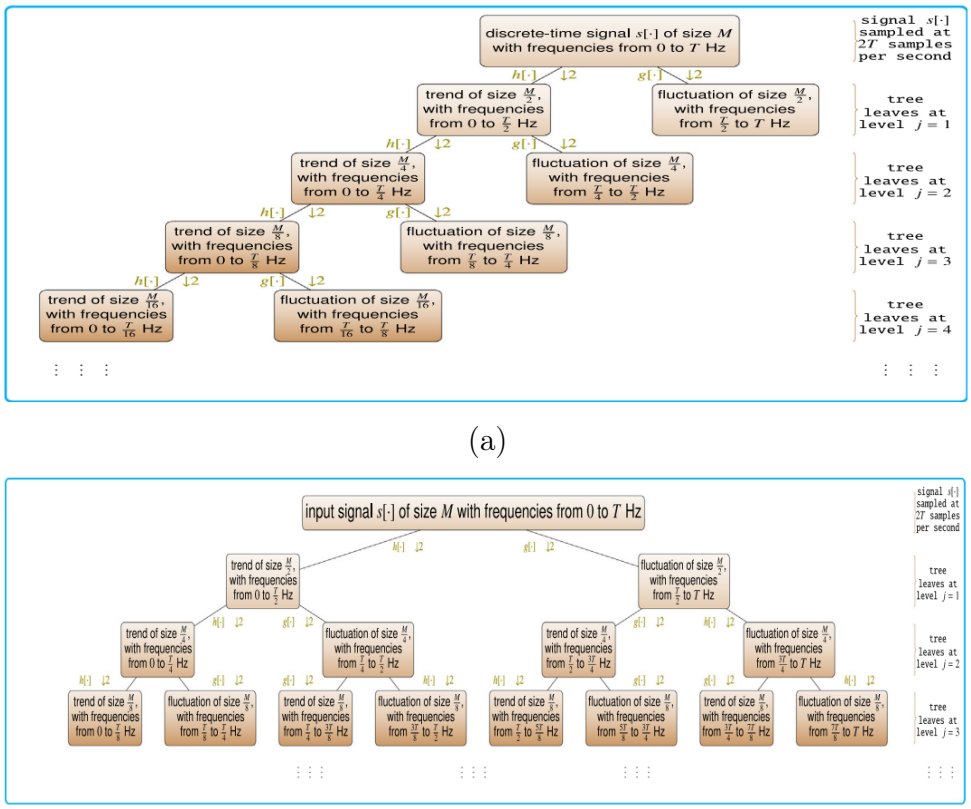

(a)

(b)

Figure 4.5: (a): DTWT decomposition tree, exemplified for a specific resolution level j=4. The downarrows represent the downsampling. (b): DTWPT structure [41].

4.2. Integration of online EIS with dynamic power profiles

Conventional methods used to perform EIS require strict operating conditions in order to provide accurate and reliable results. First, EIS tests are typically carried out under steady-state conditions using a controlled sinusoidal excitation, as described in Chapter 1. In EVs, battery operation is inherently dynamic, from the battery performance perspective, this results in continuous variations in the magnitude, sign, and slope of the current profile. In the case of offline EIS methods, the vehicle must be turned off so that the battery can reach electrochemical equilibrium before the impedance measurement is performed. In contrast, within the online EIS framework, the dynamic WLTP profile acts as the excitation source for impedance-related analysis. For this reason, the objective of the estimation is to extract information during the normal operation of the battery, without interrupting the dynamic load profile. An analysis performed while the system is operating

under normal conditions is commonly referred to as *real-time* analysis. The WLTP cycle provides a representation of a dynamic battery operating profile, simulating realistic vehicle behavior. As an example, the WLTP Class 3b cycle, which includes the majority of modern EVs, is divided into four sections: low, medium, high, and extra-high (Figure 4.6). Each section contains a variety of driving phases, stops, acceleration, and braking phases. In general, these four portions are associated with high-traffic-density urban roads for the low phase, low-traffic-density urban roads for the medium phase, suburban roads for the high phase, and highway driving conditions for the extra-high phase [43]. In this regard, the WLTP profile exhibits multiple time-scale characteristics, since dynamics occurring over different temporal ranges are superimposed within the same signal. Some variations take place slowly over several minutes and can be associated with the evolution of SOC. Other variations occur over shorter time intervals, on the order of seconds, highlighting polarization phenomena. Certain changes in the dynamic profile of the cell are even faster, occurring over a few milliseconds, and are related to resistive effects. Therefore, the WLTP signal exhibits a continuous frequency content, as it is non-stationary and characterized by frequent changes in slope. Each transition in signal evolution introduces additional frequency components; consequently, the overall profile is described by the coexistence of multiple frequencies across a broad spectrum.

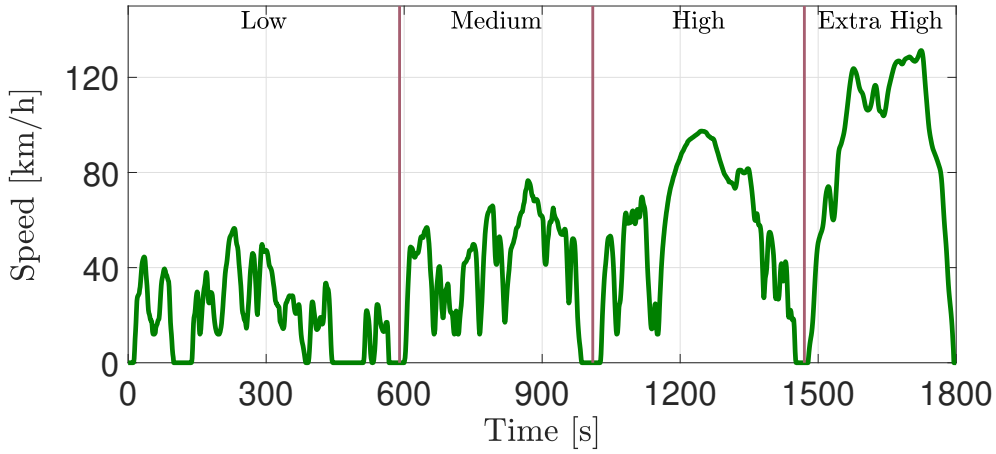

Figure 4.6: Speed-time profile of the WLTC Class 3, divided into four phases: low, medium, high, and extra high.

Traditional frequency-domain techniques, such as FTs, rely on a fundamental requirement in order to operate correctly: the analyzed signal must be stationary, meaning that its statistical properties and frequency content do not vary over time [44]. Under this assumption, the different frequencies in the signal are constant, and the amplitude

associated with each frequency component does not depend on time. These conditions are satisfied, for instance, in the case of sinusoidal signals, as well as periodic or quasi-periodic signals. In contrast, the WLTP profile does not satisfy these assumptions, since its frequency components are not constant over time and may appear, disappear, or change their intensity as operating conditions evolve. If FTs were applied to the WLTP signal, information regarding when a specific electrochemical phenomenon occurs within the cell would be lost, as this tool is not capable of detecting the time instants at which changes in the signal's frequency content take place. For the reconstruction of an impedance spectrum from a dynamic signal such as the WLTP profile, the need for time–frequency methods becomes evident. These techniques are capable of reconstructing the frequency spectrum while preserving information about the temporal localization of signal variations. Among time–frequency analysis techniques, wavelet-based approaches are particularly suitable for non-stationary signals, since they enable the simultaneous localization of signal characteristics in both time and frequency ranges. EIS provides valuable insights about the SOH of the battery and, as discussed in Chapter 1, distinct regions of the impedance spectrum can be associated with specific electrochemical processes occurring within the cell. Since these phenomena exhibit different time constants, the time–frequency domain methods enable their temporal separation without imposing stationarity assumptions that would otherwise lead to non-realistic results when analyzing dynamic profiles such as the WLTP.

The approach of this thesis is the following:

- probe the battery by injecting a signal with a complex spectrum which it is not sinuosidal (conventional techniques);
- recover the Nyquist plot by a wavelet analysis of the battery voltage and current signals.

The signals can be recorded during the normal operation of the battery, without requiring a lab or special equipments. In this thesis the signals under analysis are recorded during the standard WLTP cycle of an EV. The goal of this work is to extend wavelet-based method to the WLTP cycle, enabling real-time impedance extraction while the battery operates under dynamic driving conditions, unlocking the analysis of how usage patterns affect vehicle performance. Additionally, it is investigated whether the approach chemistry-agnostic, since it is evaluated its performance across multiple lithium-ion chemistries (e.g., NMC, LFP) to assess generalizability across battery types. The voltage and current signals shown in Figure 4.7 are relative to a single Li-ion cell as a scaled down replica of the current and voltage signals of a car battery pack.

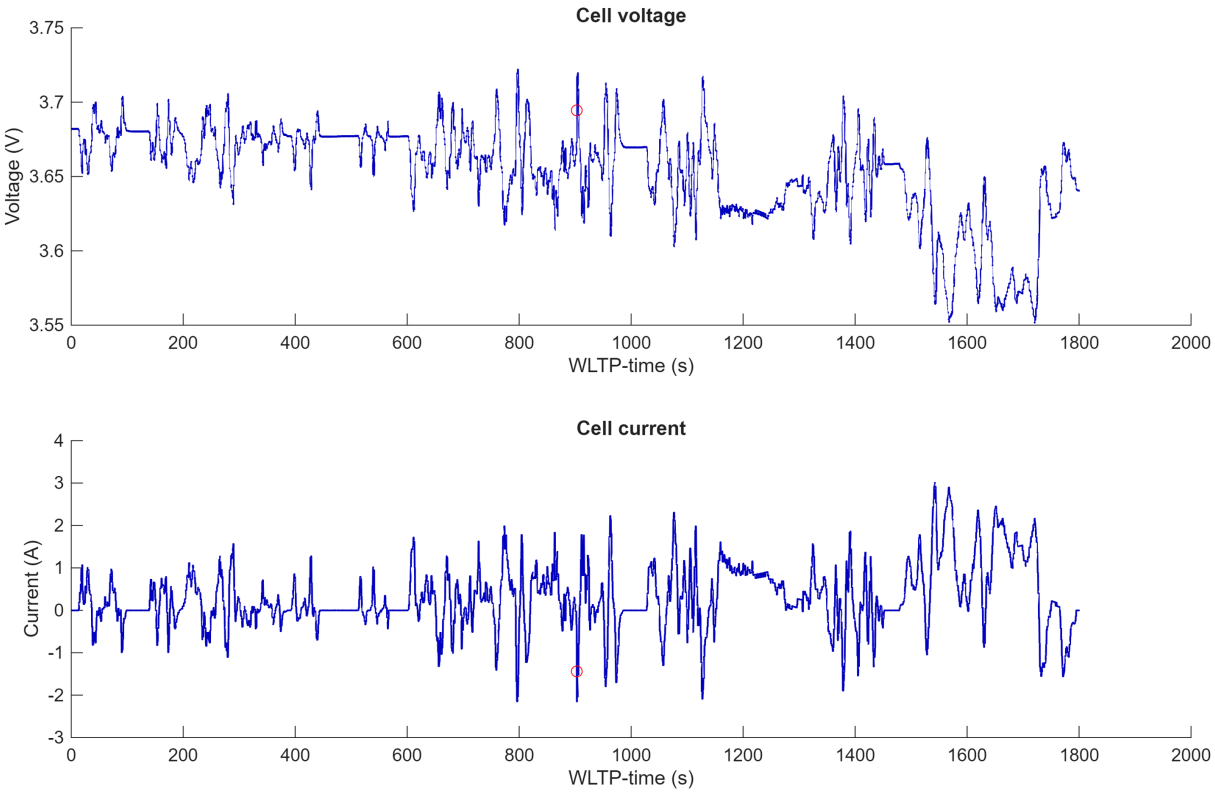

Figure 4.7: Voltage and current trend during a WLTP cycle.

4.3. Comparison framework: standard EIS and wavelet-based diagnostic method

The EIS measurements performed under laboratory conditions constitute the experimental reference for the validation of the proposed method. These measurements are carried out under controlled conditions, at predefined SOC steps, with stable and controlled temperature, and with the cell operating as close as possible to electrochemical equilibrium. The laboratory EIS measurements are performed using the technique described in Chapter 1, in which the excitation variable is the current, implemented through the GEIS technique. In this case, the excitation source is a controlled sinusoidal signal, the system is stationary, and only one frequency is applied at a time. In contrast, in online EIS the WLTP driving cycle simultaneously excites the battery over multiple time scales. Through the WT, the voltage and current signals are decomposed into components localized in both time and frequency. Wavelets isolate a frequency band, which is characterized by a frequency around which the wavelet is most sensitive referred to as *pseudo-frequency* (f_a). This term does not represent an exact frequency, as in the case of a pure sinusoid, but rather an equivalent frequency that provides indicative information about the spectrum

associated with a specific scale value (a) and a chosen sampling period (Δt) (Equation 4.7). The value of the central frequency (f_c) depends on the selected wavelet and represents the frequency at which the mother wavelet oscillates before scaling.

$$f_a \approx \frac{f_c}{a \cdot \Delta t} \tag{4.7}$$

By exploiting the current and voltage components within this frequency band, it is possible to estimate an impedance value around f_a when operating at scale a ($Z_{WT}(f_a)$), which can be directly compared with the impedance value obtained from classical EIS ($Z(f)$). Similarly to conventional methods, the wavelet-based approach isolates frequency bands associated with different electrochemical processes, thereby enabling diagnostic information that is comparable to that obtained from traditional impedance spectroscopy. The main difference with respect to these offline methods lies in the nature of the excitation source. In the case under analysis, the dynamic WLTP profile does not excite all frequencies with the same energy. As a consequence, certain regions of the impedance spectrum, such as the high-frequency domain, are estimated more accurately, since they are associated with rapid temporal variations. Conversely, impedance information at lower frequencies is more challenging to estimate reliably due to the reduced excitation content and the intrinsically slower dynamics involved.

The validation of the method proposed in this work is carried out through a comparison between the impedance spectra obtained from laboratory EIS measurements performed on the three cells and the impedance estimated using wavelet-based techniques. The first necessary step consists in verifying that the application of a single WLTP cycle with a duration of 1800 s does not significantly change the electrochemical state of the cell. This condition is essential to ensure that the impedance information extracted through the wavelet-based approach can be meaningfully compared with laboratory EIS results. To this end, for each analyzed SOC level, impedance measurements are performed both before and after the application of the WLTP cycle. To allow the cell to cool down and reach electrochemical equilibrium, at the end of the initial discharge step of 25% SOC (or 20% in the case of the final step down to 5%), the cell is left at rest for 45 minutes. At the end of this rest period, the first impedance measurement is performed. Subsequently, one cycle of the vehicle power profile associated with the cell is applied, and finally the second impedance measurement is carried out. In the case where the two EIS measurements are consistent, the experimental protocol is accepted. Conversely, when discrepancies are observed, the rest period following the discharge step is extended to allow the battery to reach conditions closer to electrochemical equilibrium.

In Figure 4.8 are illustrated the impedance spectra measured before and after the application of the Tesla power profile in the NMC cell. The comparison indicates that, following a rest period, no appreciable electrochemical variations are induced by the application of the WLTP power profile. It can be observed that, as the SOC decreases, the impedance spectrum measured after the WLTP cycle tends to progressively diverge from that obtained before the cycle. In the high-frequency region, the impedance response remains nearly identical in all cases, since the ohmic resistance is essentially independent of the SOC. Conversely, the mid-frequency semicircle, which provides information on the charge transfer resistance, exhibits a clear dependence on the SOC level. This contribution reflects the kinetics of the electrochemical reactions occurring within the cell. As the SOC decreases and polarization effects increase, the charge transfer resistance rises, leading to noticeable discrepancies between the impedance spectra, particularly starting from a SOC of approximately 50%. Under these conditions, the cathode becomes increasingly lithiated, resulting in limited lithium diffusivity and increased charge transfer resistance. This behavior is clearly visible in the Nyquist plots as a rightward shift of the red curve with respect to the blue one when moving toward lower frequencies. Moreover, the low-frequency domain, represented by the Warburg tail, is the most sensitive region to SOC variations. As a consequence in all impedance spectra, a divergence in the low-frequency response is evident and it becomes more pronounced as the SOC progressively decreases. In this range of frequencies, diffusion and lithium redistribution processes, which are intrinsically slow, manifest predominantly with respect to the high frequency section.

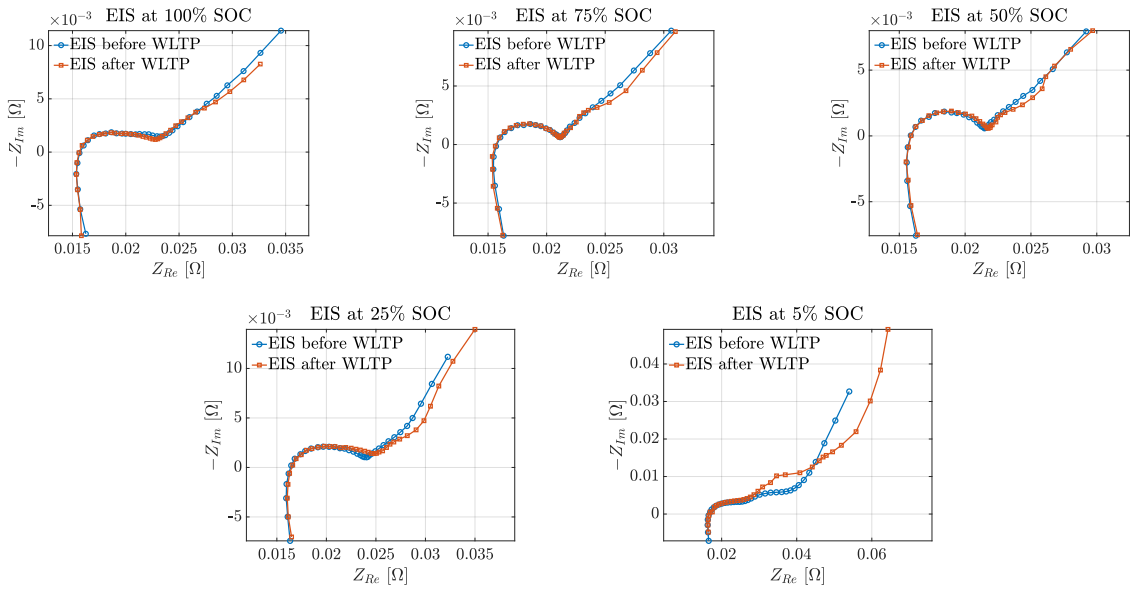

Figure 4.8: Nyquist plots of the electrochemical impedance spectra measured before and after the WLTP cycle at different SOC levels (Tesla cycle).

At high levels of charge (100%–75%), the anode is nearly fully lithiated and the cell operates under favorable electrochemical conditions. In this SOC range, the WLTP cycle does not introduce measurable variations across the entire frequency spectrum, resulting in impedance spectra that are almost perfectly overlapped. As the SOC progressively decreases, the low-frequency region of the impedance spectrum measured after the WLTP cycle diverges increasingly from the corresponding pre-cycle response. Considering the limiting case at 5% SOC, the cell operates very close to its lower operating limits and therefore exhibits a different electrochemical behavior. At such low level of charge, the anode is almost completely delithiated, leading to the formation of strong concentration gradients. Under these conditions, slow dynamic phenomena such as polarization and diffusion become dominant and are observable only at low frequencies. In this operating regime, the cell perceives the limited diffusion as a very large impedance contribution, causing a pronounced upward increase of the Warburg tail which, being far from ideal conditions, no longer exhibits its characteristic 45° slope. In addition, the mid-frequency semicircle associated with the charge transfer resistance appears to be flattened and wider, as a consequence of the overall increase in the resistance to lithium diffusion within the cell.

After performing the EIS test at different SOC levels following the application of the WLTP cycle, the comparison between the two methods is carried out. The validation of the wavelet-based method is not performed through a point-by-point comparison of the results, because the operating conditions and the excitation sources are different. Instead, the physical consistency of the two outcomes is analyzed, highlighting the compatibility of their trends and the capability of capturing the various electrochemical processes of the cell from the impedance behavior, similar to the conventional approach. In any case, online EIS is not intended to replace laboratory-based EIS, its primary purpose is to extract diagnostically consistent information during normal operation and in real time. Furthermore, the test is conducted at multiple SOC steps in order to obtain information over the entire charge range of the cell and to further strengthen the diagnostic validity of the proposed method.

5 | Results and discussion

5.1. Analysis of offline EIS results

The internal electrochemical behaviour of the cells was initially investigated through a SOC-resolved offline EIS characterization. The test procedure is described as follows:

- CC-CV charge at 0.5C and a following rest period to reach equilibrium conditions;
- EIS measurements every 10% decrease in SOC;
- additional EIS measurements at 5% SOC.

The procedure was repeated during the charging phase, moreover, before every EIS acquisition a rest period was introduced ensuring stable conditions before the measurement. This test highlights the evolution of the cell impedance as the SOC decreases or increases. Chapter 4 introduces the main mechanisms responsible for the SOC-dependent variation of the impedance response, particularly at decreasing frequencies. The offline EIS tests performed at multiple SOC steps during both charge and discharge phases highlight the evolution of the impedance response across the investigated frequency range as the SOC varies, while also enabling a comparison between the two chemistries.

Figure 5.1 shows the impedance spectra at selected SOC levels for both cells type during charge and discharge. In order to compare the curves, particular attention must be given to the low-frequency region, where the Warburg tail shifts and its slope changes with SOC in all cases. During the discharge phase of the LFP cell (Figure 5.1 (a)), at the initial fully charged state, the impedance exhibits a pronounced upward trend and it is significantly shifted to the left compared to the other SOC levels. This behavior arises because, at the beginning of discharge, the $LiFePO_4$ particles in the cathode are fully lithiated and the initial delithiation process requires nucleation of the $FePO_4$ phase together with the formation of a moving phase boundary. This two-phase transformation introduces kinetic and diffusion limitations, resulting in a pronounced impedance response in the low-frequency region (Figure 5.2). At subsequent SOC levels, the impedance evolution becomes more consistent, as the phase boundary is already established and the electrode

potential remains approximately constant.

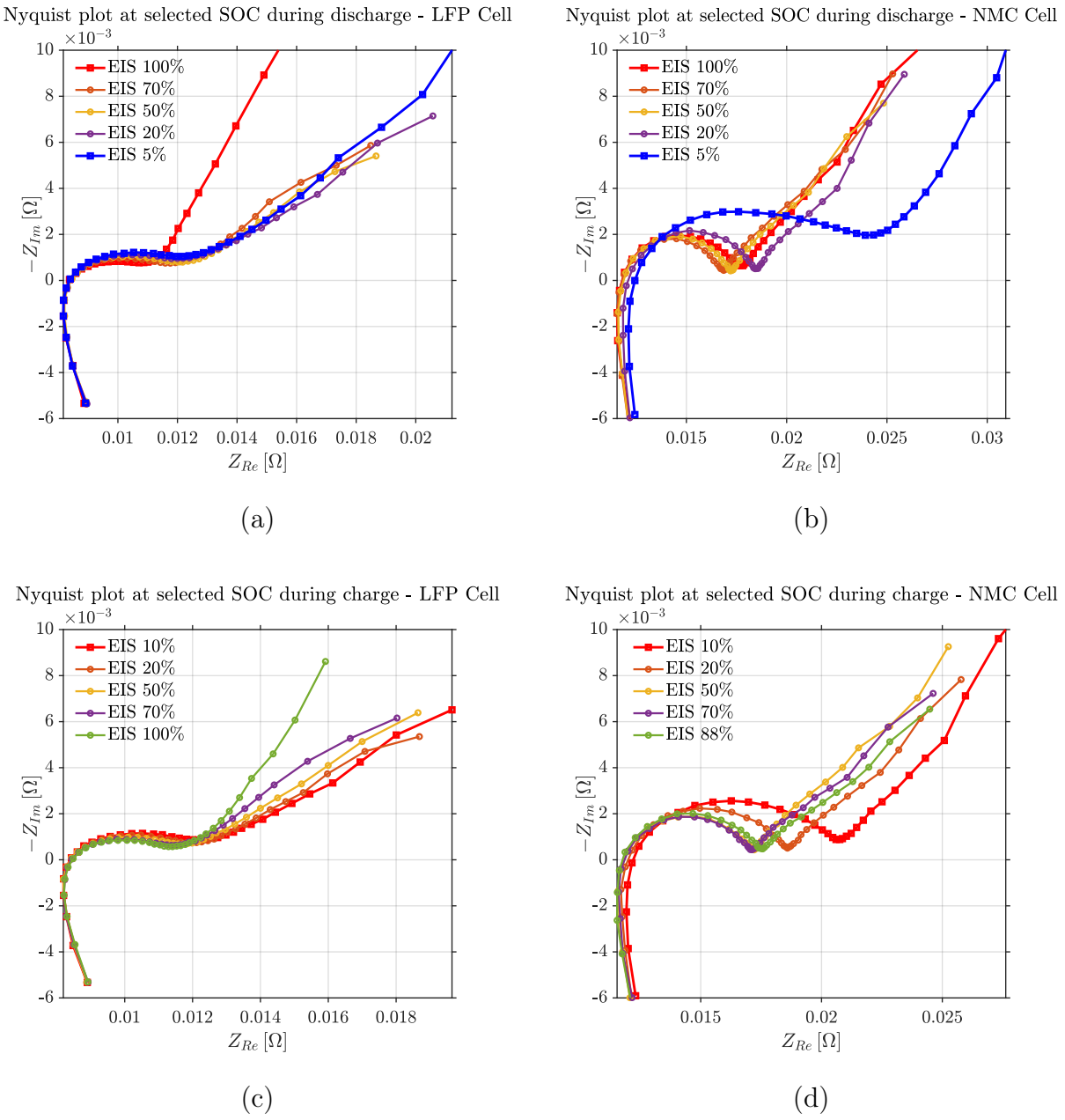

Figure 5.1: Nyquist plots during the discharge phase: (a) and (b). Nyquist plots during the charge phase: (c) and (d).

In the case of the NMC cell (Figure 5.1 (b)), the impedance curves exhibit slightly different behavior. The mid-frequency semicircle, typically associated with charge-transfer resistance and CEI-related interfacial processes, progressively shifts toward higher real impedance values as the SOC decreases. Unlike the LFP cell, the most distinct behavior

in the low-frequency region for the chemistry of NMC is observed at 5% SOC, where the spectrum becomes more isolated. This effect can be attributed to the emergence of multiple overlapping time constants related to different electrochemical phenomena, which become more pronounced at very low states of charge.

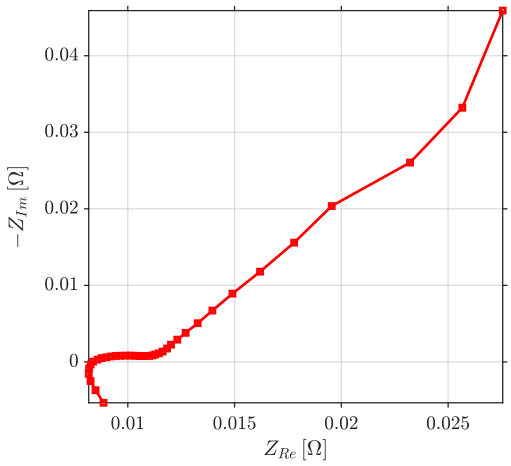

Figure 5.2: Nyquist plot of the LFP cell at 100% SOC before discharging.

During the charging phase (Figure 5.1 (c)), the LFP cell exhibits a relatively compact impedance behaviour up to a state of charge close to 100%, where a clear separation of the low-frequency tail becomes evident. In this region, the low-frequency impedance rises more rapidly for the reasons discussed above. In contrast, the NMC cell shows a less regular trend (Figure 5.1 (d)). As the SOC increases, the enhanced electrochemical activity favours the reaction kinetics, leading to a reduction in resistance and a corresponding shrinkage of the mid-frequency semicircle. However, it can be observed that the EIS spectrum at 88% SOC exhibits a larger semicircle compared to intermediate SOC levels (50% and 70%). This behaviour is attributed to increased polarization and slower charge-transfer kinetics at high SOC, which result in a higher resistance. Due to the overpotentials associated with these resistive contributions, the terminal voltage increases significantly. As a consequence, the maximum SOC reached during the charging process is approximately 88% rather than 100%, unlike in the LFP case. This behaviour is typical of this kind of cells, whose voltage–SOC relationship does not exhibit a flat plateau. In this context, even a small variation in SOC can lead to a substantial increase in potential, causing the maximum voltage limit to be reached before full charge is achieved. This test is required to represent the electrochemical processes occurring within the cell across the frequency range and to provide information regarding the characteristic time constants of the battery components.

The resulting measurements establish a reference framework that is subsequently used for the validation of the proposed online method.

A second EIS measurement campaign was carried out following the application of power profiles derived from WLTP vehicle data, with the objective of reproducing operating conditions representative of real driving dynamics. The test protocol was defined as follows:

- CC-CV fully charge at 0.5C with a following rest period of 45 minutes;
- EIS measurement;
- WLTP-based power profile of the corresponding vehicle (Tesla: NMC1; Peugeot: NMC2; Dacia: LFP), with current and voltage signals recorded with a sampling frequency of 500 Hz;
- Eis measurement;
- the procedure is repeated at the following SOC levels after a CC discharge at 0.5C: 75%, 50%, 25%, 5%.

As previously discussed in Chapter 4, the first step consists of calibrating the resting period prior to acquiring the initial EIS measurements, in order to allow the cell to reach electrochemical equilibrium. This step is essential for enabling a direct comparison between the spectra acquired before and after the WLTP profile, thereby demonstrating that the application of the driving cycle does not induce significant changes in the electrochemical structure of the cell. Ensuring this condition is crucial to guarantee that the results remain comparable with those derived from the online methodology. The offline EIS spectra of the Tesla profile are already presented in the final section of Chapter 4. For completeness, the corresponding offline EIS results for the Peugeot and Dacia cycles are reported in Appendix A to preserve readability and avoid redundancy within the main discussion.

5.2. Validation of the wavelet-based online method

The validation of the proposed online EIS estimation method is carried out by comparing the results obtained from conventional offline laboratory EIS measurements with those derived from the wavelet-based approach. The objective is not to replicate classical EIS, but rather to identify the internal electrochemical processes of the batteries within the frequency response extracted under dynamic conditions. The comparison was performed with reference to the impedance spectra obtained at different SOC steps under excitation by the corresponding WLTP-based power profiles. As discussed in Chapter 4, WTs, unlike

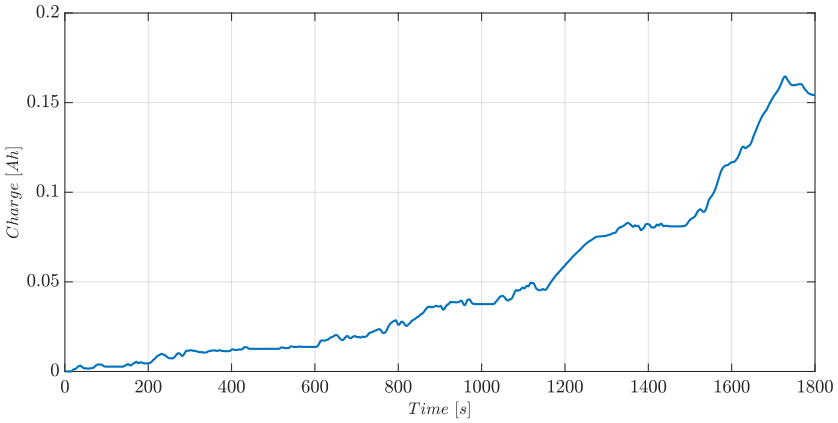

Figure 5.3: Cumulative charge extracted from battery during WLTP.

FTs, provide time–frequency localization, enabling the identification of when specific frequency components occur in time. This property allows the differentiation of distinct electrochemical phenomena within the same spectrum under non-stationary excitation. The signals are synchronously sampled at 500 Hz, and the maximum frequency that can be observed in the Nyquist plot is 250 Hz, as already described in Chapter 3. The minimum frequency instead is related to the duration of the signals, since one period of 1800s means frequencies in the order of millihertz. Figure 5.3 shows the cumulative charge extracted during the WLTP cycle. Knowing the starting SOC and the battery Ah capacity, it is possible to calculate the SOC(t) at each instant during WLTP as:

$$SOC(t) = SOC_0 - \frac{Q_{extracted}(t)}{Q_{nom}} \tag{5.1}$$

In order to mimics EIS by signal processing, the spectrum of voltage and current is computed as a function of time and the instant at which recover a Nyquist plot is decided. Therefore, it is necessary to perform a time-frequency analysis of signals and calculate a corresponding spectrogram. The goal is to achieve a good resolution in time and frequency, which is a conflicting requirement. To carry out the analysis, it is necessary to use a wavelet that is finite in both time and frequency. For this purpose, the Generalized Morse Wavelet was selected. The voltage and current spectrograms were computed using the CWT. At this point, it is possible to obtain a Nyquist plot at each instant of the WLTP cycle, which contains a rich frequency spectrum. The example shown in Figure 5.4 presents six three-dimensional Nyquist plots, each selected within a 300 s window. The filled circles correspond to regenerative braking events, when the battery is being recharged.

Figure 5.5 presents the final results of this work, that is the comparison between conventional EIS and the wavelet-based impedance estimation for the three power profiles.

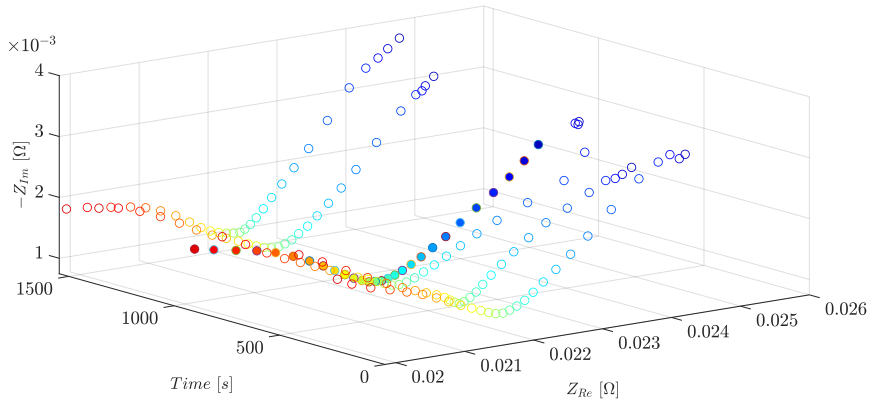

Figure 5.4: CWT Nyquist plots during WLTP.

The colored markers, where red corresponds to the highest analyzed frequency and blue to the lowest, represent the impedance values extracted through the wavelet transform. The results do not span the entire frequency range of classical EIS, but rather the frequency interval that is meaningful for the considered application. The upper frequency limit is inherently constrained by the sampling frequency of the excitation signal, as previously discussed. The lower frequency boundary, however, is determined by the characteristics of the wavelet functions. As the analyzed frequency decreases, the wavelets become increasingly stretched in time, allowing the capture of slower dynamics. If excessively low frequencies are considered, the corresponding wavelet functions may overlap significantly, potentially leading to a loss of resolution and reduced reliability of the extracted impedance information. For clarity, the discussion focuses on three representative SOC levels (100%, 50% and 5%), while the results for the remaining charge steps are reported in Appendix A.

From the Nyquist plots shown in Figure 5.5, it is possible to identify a clear similarity in the impedance patterns obtained from conventional offline laboratory measurements and those derived through the wavelet-based approach. Indeed, the latter is able to reproduce the overall trend of the reference spectrum with good agreement. As previously discussed, the EIS from the wavelet method does not cover the entire frequency range, however, this limitation does not represent a critical issue in real-world applications. In this regard, as highlighted by the results, the online EIS estimation provides consistent information within the mid-frequency region. The latter, instead, represents very slow processes, while the WLTP driving cycle is characterized by continuously varying current and voltage profiles. Under such dynamic conditions, the wavelet transform is unable to clearly separate extremely slow dynamics, and the estimation of reliable parameters would require excessively long observation windows. The mid-frequency region, however, represents the

core of LIB diagnostics. In this frequency band, the charge-transfer resistance dominates and shows strong sensitivity to variations of direct indicators of battery condition as temperature, SOC, and SOH. In conclusion, the wavelet-based EIS estimation proves to be a valid approach for extracting impedance related information online. Since the WLTP cycle represents a realistic driving profile, the proposed method can be applied to real vehicles without the need to inject artificial excitation signals.

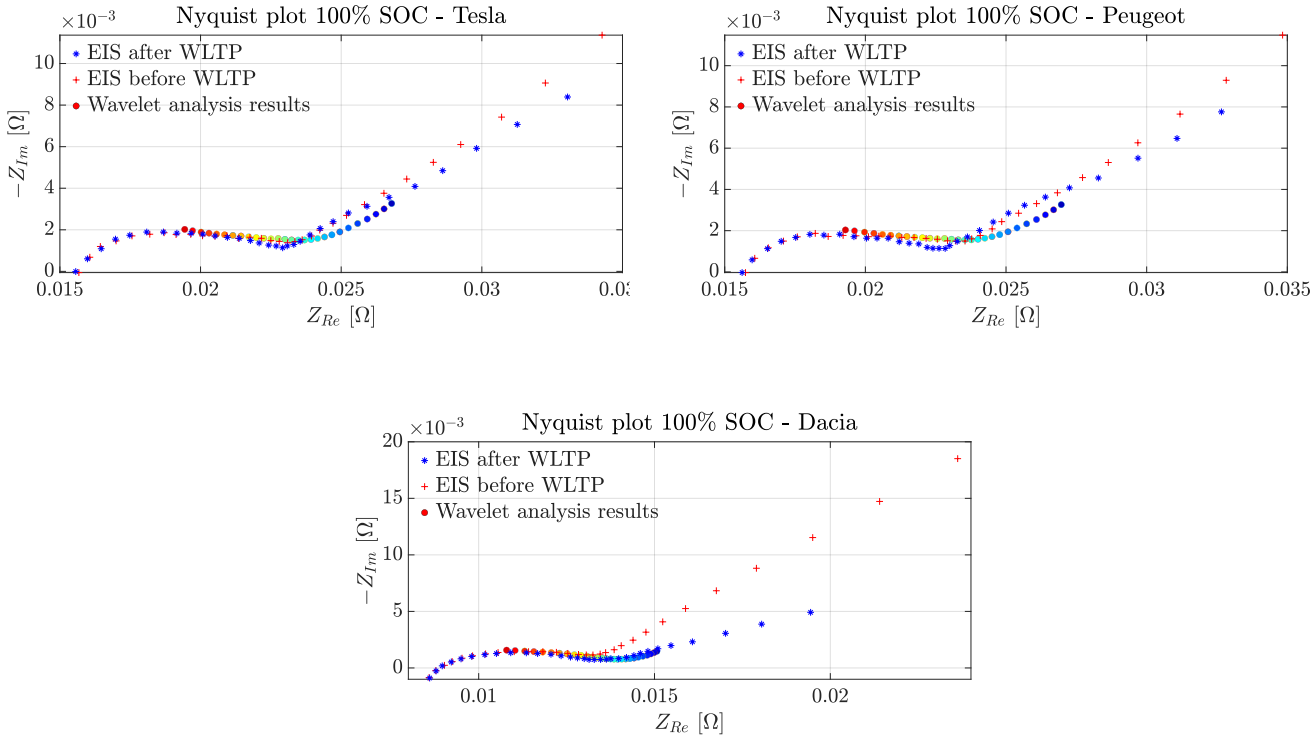

(a)

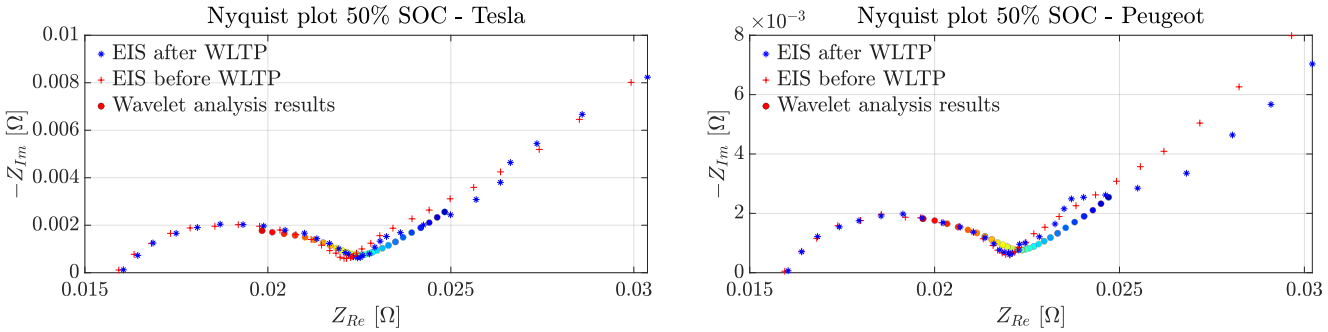

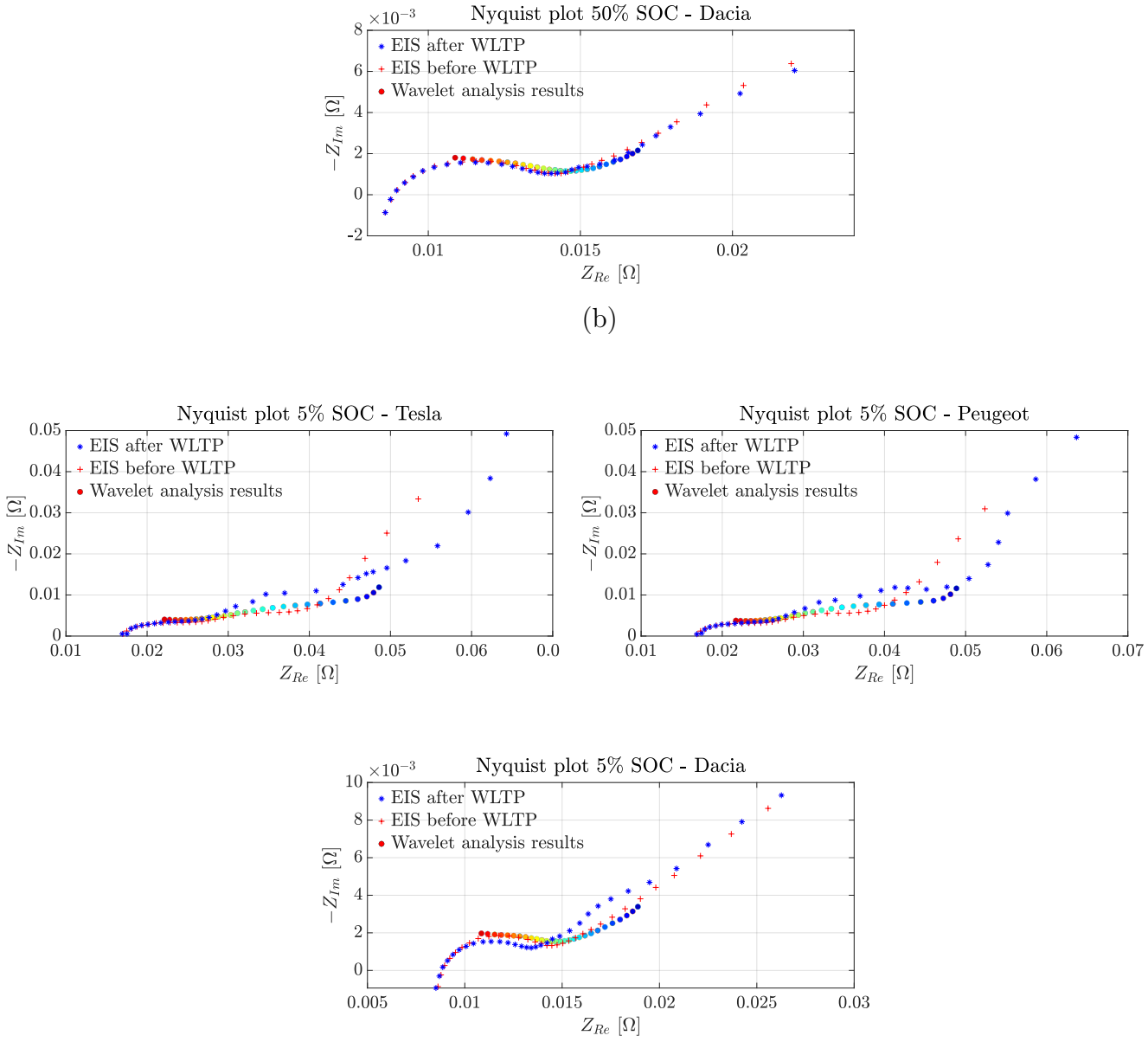

Figure 5.5: Comparison of offline EIS measurements and wavelet-based online impedance estimation at different SOC levels for the three EVs: (a) 100%, (b) 50%, and (c) 5%.

5.3. LFP specific analysis: peak identification and tracking

As previously introduced in the final section of Chapter 3, the first step in the DVA analysis used in this work consists of obtaining an OCV(SOC) curve. This profile is

derived from the first test described in Section 5.1, where an OCV value is computed at each discharge SOC step by averaging the last data points recorded during the rest phase. The continuous profile is obtained using the shape-preserving piecewise cubic Hermite polynomial (pchip) function in MATLAB (Figure 5.6). This tool preserves the monotonic behavior of the profile and it also avoids artificial oscillations providing stability and accuracy.

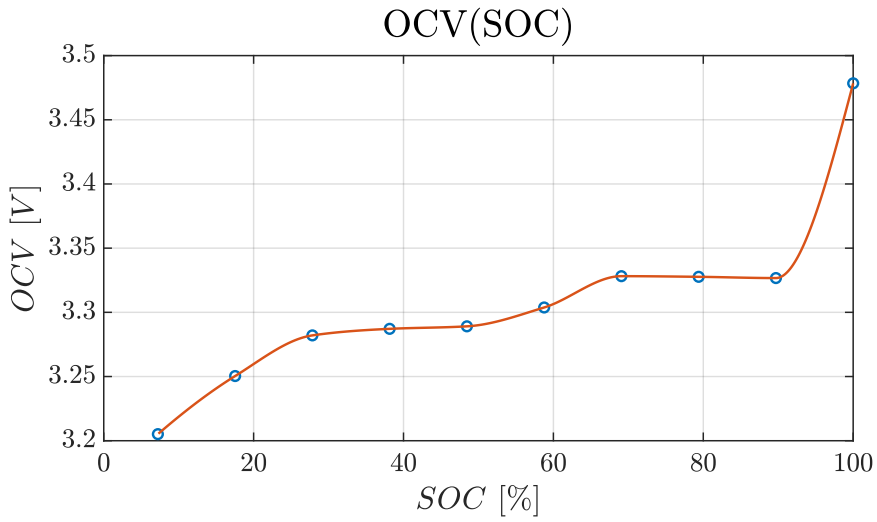

Figure 5.6: Experimental OCV(SOC) curve obtained from stepwise measurements.

At this stage, the derivative of the OCV with respect to SOC is computed (Figure 5.7), and the electrochemical peaks are extracted using MATLAB's *findpeaks* function. As shown in the plot, only one clearly stable peak is identified, located at 62.80% SOC. This value is particularly significant, as it corresponds to the point at which the cell reaches a phase-equilibrium condition. From a diagnostic perspective, this peak represents a key feature, since it consistently appears at the same SOC level, although it tends to shift as battery aging progresses. Therefore, even in aged cells, this landmark can be used as a reference point for estimating SOH and assessing the internal condition of the battery. The figure also exhibits steep increases at very low and very high SOC regions. This behavior is consistent with the shape of the OCV curve, where the voltage decreases outside the plateau region. The peak extracted from this curve is used as a landmark for SOC estimation under dynamic driving conditions such as the WLTP cycle. From the WLTP standpoint, the power profile associated with the Dacia vehicle has been repeatedly applied until the cell, starting from a fully charged state, is completely discharged and reached the minimum voltage threshold, which for the investigated cell is 2 V. The resulting voltage and current profiles measured during this test are shown in Figure 5.8 (a) and (b) respectively. The DVA is performed on a quasi-OCV voltage profile

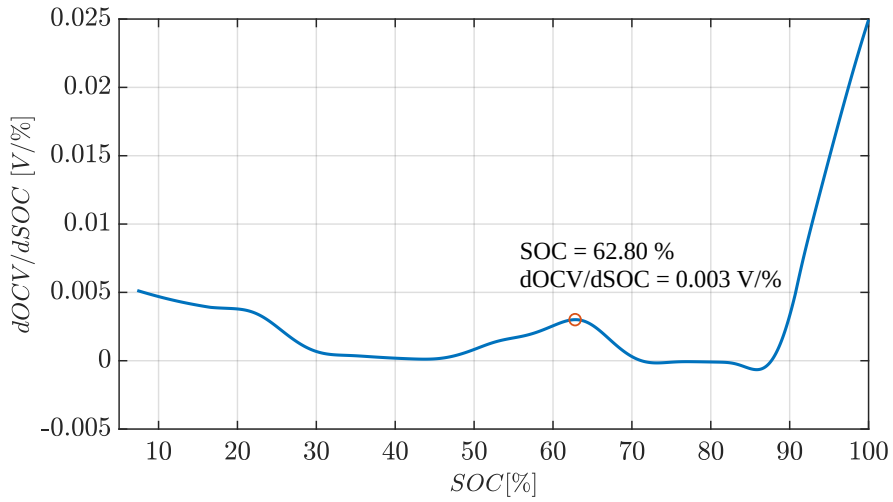

Figure 5.7: Differential open-circuit voltage curve $dOCV/dSOC$ as a function of SOC with the identified electrochemical peak highlighted.

obtained by removing the voltage drop contribution associated with the internal resistance. The series resistance R_0 used in the ECM was directly identified from EIS measurements. Specifically, this resistance corresponds to the high-frequency intercept of the Nyquist plot, which represents the intrinsic ohmic resistance of the cell. This contribution includes the electrolyte resistance, current collectors, and contact resistances, and it accounts for the instantaneous voltage drop under load. The experimentally extracted value of $20m\Omega$ was therefore adopted as the series resistance in the model. Figure 5.8 (c) shows the corrected profile compared to the measured terminal voltage obtained during the test. The voltage corrected for the resistive voltage drop is referred to as quasi-OCV because it cannot be directly compared to a pure OCV measurement. In fact, it still includes kinetic polarization effects, diffusion contributions, and transient phenomena induced by the WLTP driving profile. By removing the resistive component, the high-frequency contribution of the impedance is effectively filtered out, allowing slower dynamics to emerge while preserving relevant dynamic information. This operation results in a more stable and balanced voltage evolution, facilitating the subsequent identification of electrochemical peaks. However, this quasi-OCV curve still exhibits several oscillations that are intrinsically linked to the dynamic nature of the driving profile and should not be mistaken for genuine electrochemical features. In the following, the corrected voltage profile is denoted as V_{corr}:

$$V_{corr} = V_{WLTP} - I_{WLTP}R_0 \tag{5.2}$$

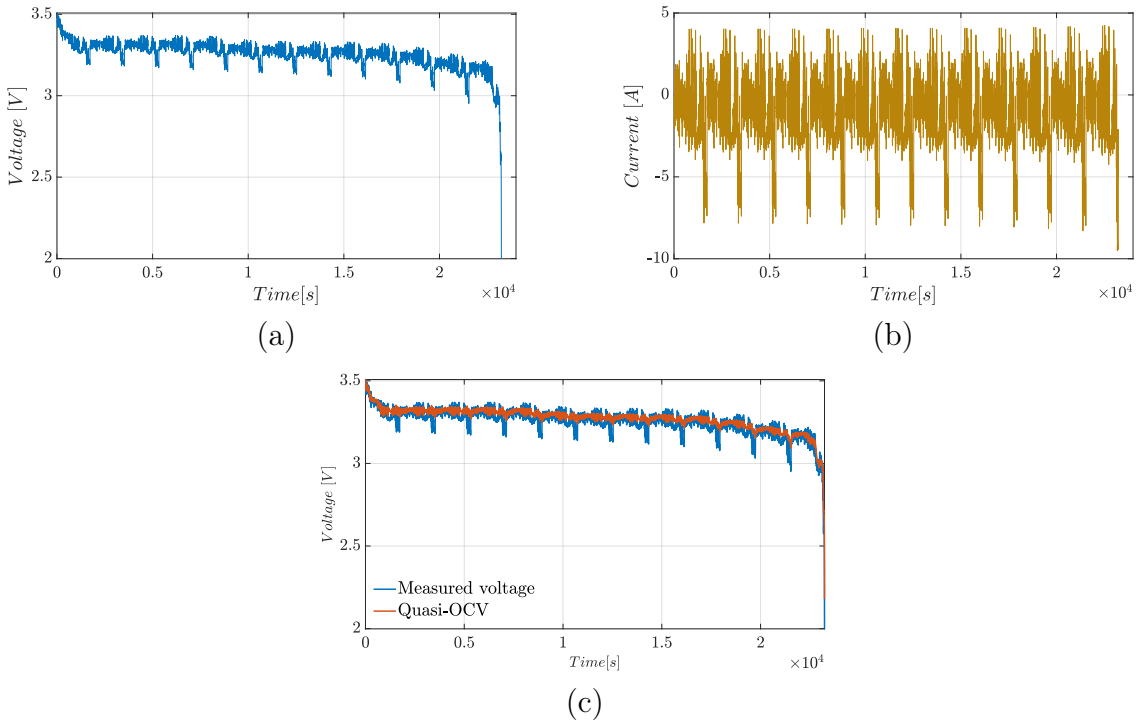

Figure 5.8: Profiles under load from WLTP cycles: voltage (a) , current (b). Comparison between measured load voltage and quasi-OCV signal, derived from ohmic-drop compensation along the WLTP profile (c).

At this point, two methods were implemented to extract the differential voltage peak: a robust bin-averaged DVA and an interpolated signal-filtered DVA.

5.3.1. Bin-averaged DVA approach

In this first method, SOC is discretized using bins with a width of 0.1% over the range from 0% to 100%. Each bin has been considered valid only if it contains at least 40 points. Subsequently, the voltage values within each valid bin are averaged. The use of a minimum number of points per bin prevents bins with very few samples from generating random voltage values. This aspect is particularly relevant for highly dynamic profiles, where voltage values are not uniformly distributed across SOC. At this stage, a discrete $V(SOC)$ curve is obtained, where each point represents a statistical average of multiple real samples. To obtain a continuous and smooth curve, the discretized voltage profile is first interpolated over the SOC range and then smoothed using the LOESS method in MATLAB. This step is fundamental because differentiation would otherwise strongly amplify the residual noise in the profile. The derivative is then computed using the MATLAB gradient function, which returns the slope of the curve point by point. For internal points, a central difference

scheme is applied, while forward or backward differences are used for boundary points.

$$\frac{dV}{dSOC}\Big|_i \approx \frac{V_{i+1} - V_{i-1}}{SOC_{i+1} - SOC_{i-1}} \tag{5.3}$$

An additional smoothing process is applied to the derivative in order to obtain a cleaner curve with reduced residual noise. At this stage, electrochemical peaks are identified using the findpeaks tool, similarly to the OCV case. This tool allows the identification of structures that exhibit actual peak characteristics, avoiding the selection of a simple global maximum that could represent an artifact. To obtain a meaningful output, it was necessary to define a minimum prominence and a minimum distance between peaks. The former represents how much a point stands out relative to the surrounding minima, highlighting not only its amplitude but also the features that make it isolated and significant with respect to the rest of the curve. In this work, a minimum prominence value of $1 \cdot 10^{-4}$V/% was imposed, representing a robust threshold that filters residual noise without losing information about the main peak. Regarding the minimum distance between peaks, a limit of 3% SOC was imposed to avoid interpreting two maxima belonging to the same physical peak as separate phenomena. In this way, two vectors were obtained: one containing the peak heights ($V/\%$) and another containing the peak positions in terms of SOC (%). Finally, the electrochemical feature was searched within the SOC range from 40% to 80%, since at very low and very high SOC values the curve assumes asymptotically high values that are not useful for the analysis. Therefore, the peak with the maximum amplitude among those detected within the selected window was chosen. The final DV curve obtained from the WLTP profile and the selected peak are shown in Figure 5.9. The resulting curve exhibits a smooth behavior and allows the peak in the selected region to be easily identified.

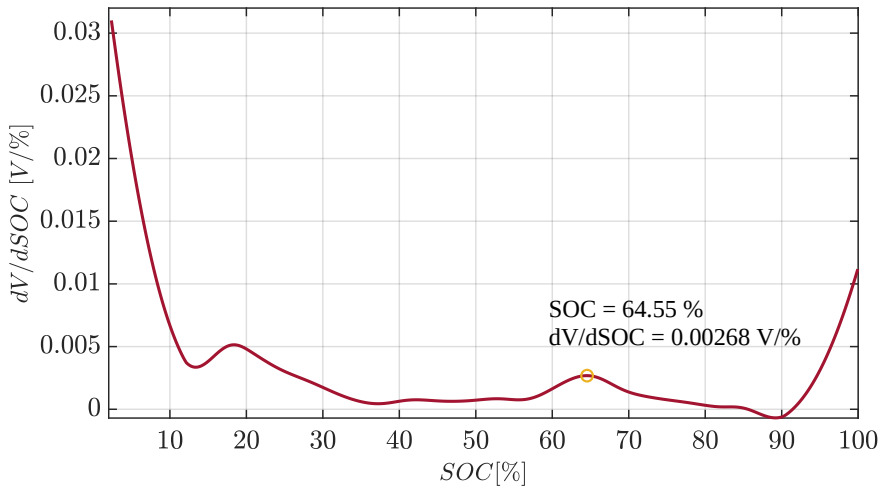

Figure 5.9: DV curve obtained from the WLTP profile with the identified electrochemical peak highlighted.

Overall, the bin-averaged method ensures high robustness and repeatability in electrochemical peak detection. It represents an effective combination of statistical aggregation with smoothing techniques, making the approach well suited for real-world datasets.

5.3.2. Interpolated signal-filtered DVA approach

The second method investigated in this work adopts a computationally less complex approach. The first step consists of reorganizing the data as a function of SOC. Since the driving cycle data are not uniformly distributed along the SOC range, the voltage previously corrected for the resistive contribution is interpolated onto a regular grid with a step of 0.1%. Once the $V(SOC)$ curve is constructed, smoothing is applied using a moving average filter with a window of 100 samples. The moving average acts as a filter that replaces each point in the signal with the average of the surrounding values. Considering a 0.1% step, this window corresponds to approximately 10% SOC, meaning that each point of the curve represents the average voltage over a local interval of about $\pm 5\%$. This width allows high-frequency oscillations caused by current transients and noise to be attenuated while preserving the overall trend of the curve. At this stage, the resulting curve exhibits a smooth and regular behavior. In this approach, the derivative is computed by evaluating the voltage variation between consecutive points of the curve, providing a discrete estimate of the derivative with respect to SOC. Since differentiation significantly amplifies noise, the derived signal is further smoothed using a second moving average with a window of 10 samples. This window performs a lighter smoothing equivalent to approximately 1% SOC.

The final trend of $dV/dSOC$ is represented in Figure 5.10. At this point, the DV curve of the corrected voltage for the WLTP cycle is obtained, and the peak calculation can be performed.

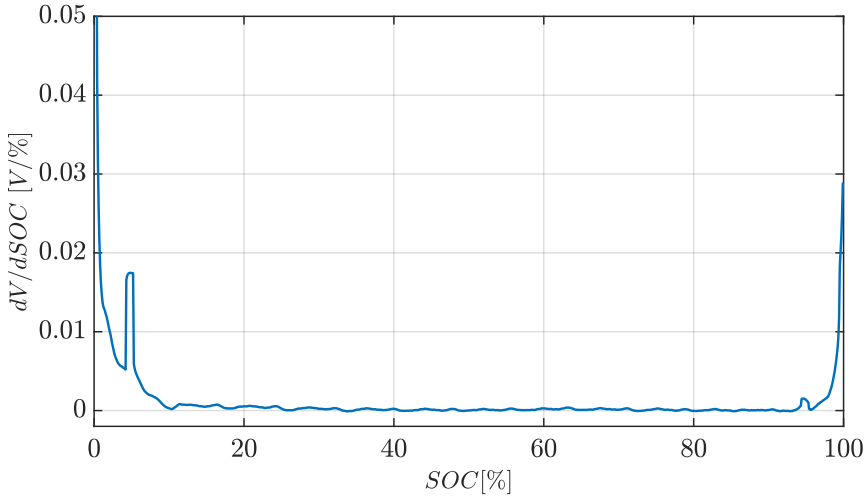

Figure 5.10: Smoothed $dV/dSOC$ trend.

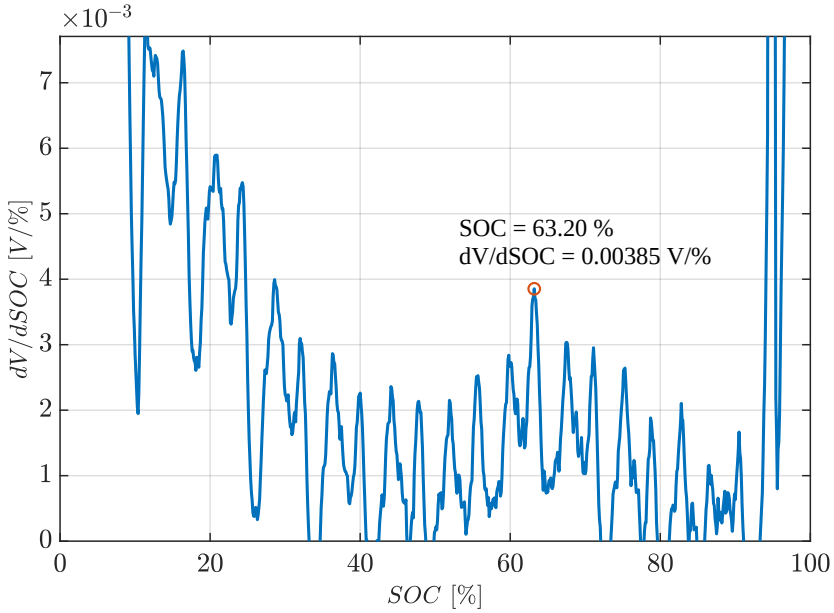

Figure 5.11: Zoomed view of the $dV/dSOC$ curve highlighting the electrochemical peak within the region of interest.

To identify the electrochemical feature of interest, the search is again restricted to the SOC range of 40–80%. Given the behavior of the smoothed curve, it is sufficient to identify the maximum point within the selected SOC interval, which corresponds to a clear

electrochemical peak relative to the surrounding points. The final trend of the voltage derivative showed in Figure 5.10 exhibits small high-frequency oscillations, resulting in an almost flat behavior over most of the SOC range. Under these conditions, the peak does not appear clearly. For this reason, Figure 5.11 shows a zoomed view of the curve in the region where the identified electrochemical signature is located. Overall, the signal-filtered method offers a straightforward implementation with low computational cost, but also exhibits poor robustness due to its sensitivity to filtering choices.

5.3.3. Comparative analysis of the implemented methods

Both methods show consistent results with each other. However, the approaches exhibit different characteristics at the implementation level. Therefore, a comparative analysis between the two methodologies was carried out. They mainly differ in terms of robustness, noise sensitivity, computational complexity, and physical interpretability of the extracted peak. The following table summarizes the main advantages and limitations of the two proposed techniques.

Table 5.1: Qualitative comparison of bin-averaged and signal-filtered DVA approaches.

Aspect	Bin-Averaged DVA	Signal-Filtered DVA
Noise robustness	High	Moderate
Sensitivity to sampling non-uniformity	Low	High
Peak detection accuracy	High	Moderate
Sensitivity to parameter tuning	Moderate	High
Computational complexity	Moderate	Low
Physical interpretability	High	Moderate
Accuracy under real driving conditions	High	Moderate

6 | Conclusions and perspectives

6.1. Final remarks on diagnostic accuracy

This work investigated the feasibility of a methodological framework aimed at extracting impedance-related information in real time under realistic driving conditions using wavelet-based analysis. An additional objective was to compare the applicability and the results obtained with those from conventional offline impedance measurements. As discussed in Chapter 5, the comparison between the two approaches demonstrates a strong physical correlation within the analyzed frequency range. Despite the intrinsic limitations imposed by the dynamic nature of the excitation profile and by signal sampling constraints, the method successfully captured the electrochemical signatures associated with SOC variations under WLTP operation. The main limitations of the proposed approach are related to the restricted frequency bandwidth and the reduced observability of very low-frequency processes. However, these aspects do not compromise the reliability of the methodology, since the most informative impedance features lie within the analyzed range. Furthermore, the DVA applied to the LFP cell enabled the identification of a stable electrochemical peak, allowing the SOH to be analyzed using a physically meaningful event. The two approches investigated are able to find valid results from a diagnostic point of view. Both of them present several advantages that make the analysis very safe and reliable. However, it is also necessary to take into account the limitations due to the algorithm itself. Anyway, in the diagnostic field of LIBs both of them could be very useful for an easy tracking of electrochemical features. In conclusion the main limitation of these methodologies lies in the complexity of identifying peaks under highly dynamic profiles, such as real driving cycles, where peak detection may not always be possible. Nevertheless, the proposed landmark selection strategy demonstrates sufficient robustness to operate under strongly dynamic conditions.

Overall, the studies presented in this work establish a physically consistent and reliable framework for online diagnostics of lithium-ion batteries, demonstrating that key impedance information can be extracted during normal vehicle operation without the need for

dedicated excitation signals. Moreover, the identification and study of significant peaks under dynamic profiles for an accurate analysis of the SOH is validated.

6.2. Impact on Battery Management System

A system called BMS is used to control batteries and optimize their performance. As shown in Figure 6.1, the BMS represents the central interface between the battery pack and the powertrain of an EV. This includes several units, each with its own function, such as cell voltage balancing, temperature monitoring, and communication interfaces. The first refers to the action through which the BMS continuously measures the voltage of individual cells in order to keep them at the same level. Within a battery pack, cells are connected in series and, since they are not perfectly identical, they may exhibit different voltage levels and therefore degrade over time in a non-uniform manner. The second function of the BMS mentioned above refers to the use of sensors to monitor the temperature of both individual cells and the entire battery pack. This parameter must be carefully controlled because it can affect safety, charging speed, and also the aging of the device. In this regard, if the temperature falls outside the allowable range, the BMS reduces the charge/discharge current and activates cooling or heating systems, thereby improving the lifetime of the device. Finally, regarding communication interfaces, the BMS must be connected to other systems in order to be diagnostically useful. These interfaces are necessary to transmit information about the battery state (SOC, SOH, temperatures, voltages) [45].

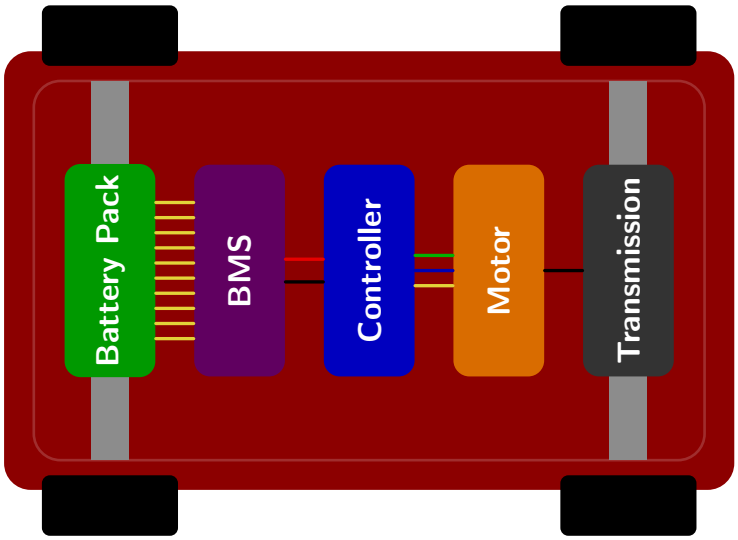

Figure 6.1: Schematic representation of the electric vehicle powertrain architecture.

The findings of this work may have significant implications for the evolution of next

generation BMS, particularly in the context of real-time diagnostics and advanced state estimation. Traditional BMS architectures mainly rely on equivalent circuit models and empirical lookup tables, which provide reliable measurements but at the same time offer limited observability of the electrochemical processes governing battery behavior. The integration of the wavelet-based method for online impedance estimation introduces a new perspective on diagnostics without the need to use artificial excitation signals. The possibility of extracting impedance components within the frequency range excited by the operating signal can significantly improve SOH estimation. Moreover, the identification of electrochemical peaks from the DV curves of the LFP cell permits a more accurate study on the SOH of the cell. In this way, it is possible to estimate the level of degradation using the electrochemical signatures found under real driving cycles. From an operational point of view, advanced diagnostic techniques, such as those presented in this work, enable the use of more adaptive control strategies. Furthermore, this approach allows a significant improvement also in thermal management, since a traditional BMS generally relies on conservative strategies to monitor temperature and it is unable to extract information at the electrochemical level. The advantage that this method would bring in this sense is the possibility of tracking the evolution of internal resistance online, allowing the anticipation of thermal behavior based on the real internal state of the cell and achieving much more precise thermal management. The last important function that can be significantly improved by the study presented is the accurate prediction of battery degradation. In this case as well, conventional BMS generally estimate the evolution of battery SOH through empirical models, that is, using indirect methods, which may lead to significant inaccuracies with respect to the true aging state. The use of wavelet-based online EIS allows direct observation of impedance variations in the charge transfer region, overall resistance increase, and possible diffusion-related changes. In this regard, the use of the proposed method would allow a more accurate estimation of battery degradation over time. In summary, the impact that such technology can have on a fundamental system such as the BMS may represent a turning point for diagnostics in the electric mobility sector.

6.3. Future research directions

The study carried out in this thesis represents a starting point for increasingly advanced technologies in the field of lithium-ion battery diagnostics. Several research directions may arise from this work. First, the extension of the wavelet-baased approach to aged cells can be investigated in order to evaluate whether the consistency between the measurements remains valid. Furthermore, different dynamic profiles can be used to identify changes related to the type of excitation. Future studies may also focus on integrating the wavelet-

based method with observers or machine learning techniques, in order to improve state estimation and real-time fault detection. From a practical perspective, it would be possible to investigate how to include online EIS analysis within BMS hardware, optimizing the computational complexity associated with wavelet processing. From a DVA perspective, the methods introduced could be further enhanced and improved. The main objective could be to develop a model capable of identifying these peaks in real time and using them to recalibrate the state of charge. By knowing the SOC at the peak, it becomes possible to recalibrate all subsequent SOC estimates.

In conclusion, the purpose of this work is to validate advanced diagnostic methods in the electric vehicle sector, in order to make the instrumentation increasingly efficient and the obtained data increasingly accurate.

Bibliography

[1] F. Sciatti, P. Tamburrano, E. Distaso, R. Amirante, A. V. Radogna, A. Morciano, and G. Grassi, "A comprehensive overview of lithium-ion batteries for electric vehicles: Materials, performance, safety, recycling, and emerging technologies," *Journal of Energy Storage*, vol. 144, p. 119694, Jan. 2026.

[2] P. Nzereogu, A. Omah, F. Ezema, E. Iwuoha, and A. Nwanya, "Anode materials for lithium-ion batteries: A review," *Applied Surface Science Advances*, vol. 9, p. 100233, June 2022.

[3] K. Mizushima, P. C. Jones, P. J. Wiseman, and J. B. Goodenough, "LixCoO2 (0<x<-1): A new cathode material for batteries of high energy density," *Materials Research Bulletin*, vol. 15, pp. 783–789, June 1980.

[4] M. Wohlfahrt-Mehrens, C. Vogler, and J. Garche, "Aging mechanisms of lithium cathode materials," *Journal of Power Sources*, vol. 127, pp. 58–64, Mar. 2004.

[5] N. Yabuuchi and T. Ohzuku, "Novel lithium insertion material of LiCo1/3Ni1/3Mn1/3O2 for advanced lithium-ion batteries," *Journal of Power Sources*, vol. 119-121, pp. 171–174, June 2003.

[6] N. Nitta, F. Wu, J. T. Lee, and G. Yushin, "Li-ion battery materials: present and future," *Materials Today*, vol. 18, pp. 252–264, June 2015.

[7] J. Wang, Z. Sun, and X. Wei, "Performance and characteristic research in LiFePO4 battery for electric vehicle applications," in *2009 IEEE Vehicle Power and Propulsion Conference*, pp. 1657–1661, Sept. 2009. ISSN: 1938-8756.

[8] X. Chen, W. Shen, T. T. Vo, Z. Cao, and A. Kapoor, "An overview of lithium-ion batteries for electric vehicles," in *2012 10th International Power & Energy Conference (IPEC)*, pp. 230–235, Dec. 2012. ISSN: 1947-1270.

[9] S. Evro, A. Ajumobi, D. Mayon, and O. S. Tomomewo, "Navigating battery choices: A comparative study of lithium iron phosphate and nickel manganese cobalt battery technologies," *Future Batteries*, vol. 4, p. 100007, Dec. 2024.

[10] C. R. Birkl, M. R. Roberts, E. McTurk, P. G. Bruce, and D. A. Howey, "Degradation diagnostics for lithium ion cells," *Journal of Power Sources*, vol. 341, pp. 373–386, Feb. 2017.

[11] J. S. Menye, M.-B. Camara, B. Dakyo, J. S. Menye, M.-B. Camara, and B. Dakyo, "Lithium Battery Degradation and Failure Mechanisms: A State-of-the-Art Review," *Energies*, vol. 18, Jan. 2025. Company: Multidisciplinary Digital Publishing Institute Distributor: Multidisciplinary Digital Publishing Institute Institution: Multidisciplinary Digital Publishing Institute Label: Multidisciplinary Digital Publishing Institute Publisher: publisher.

[12] X. Liu, Z. Hu, X. Wang, and M. Xie, "Capacity Degradation Assessment of Lithium-Ion Battery Considering Coupling Effects of Calendar and Cycling Aging," *IEEE Transactions on Automation Science and Engineering*, vol. 21, pp. 3052–3064, July 2024.

[13] M. Petit, E. Prada, and V. Sauvant-Moynot, "Development of an empirical aging model for Li-ion batteries and application to assess the impact of Vehicle-to-Grid strategies on battery lifetime," *Applied Energy*, vol. 172, pp. 398–407, June 2016.

[14] M. Ecker, J. B. Gerschler, J. Vogel, S. Käbitz, F. Hust, P. Dechent, and D. U. Sauer, "Development of a lifetime prediction model for lithium-ion batteries based on extended accelerated aging test data," *Journal of Power Sources*, vol. 215, pp. 248–257, Oct. 2012.

[15] J. Nájera Álvarez, *Study and Analysis of the Behavior of LFP and NMC Electric Vehicle Batteries concerning their Ageing and their Integration into the Power Grid*. PhD Thesis, Universidad Politécnica de Madrid, Dec. 2020.

[16] Y. Cui, P. Zuo, C. Du, Y. Gao, J. Yang, X. Cheng, Y. Ma, and G. Yin, "State of health diagnosis model for lithium ion batteries based on real-time impedance and open circuit voltage parameters identification method," *Energy*, vol. 144, pp. 647–656, Feb. 2018.

[17] M. Dubarry and B. Y. Liaw, "Identify capacity fading mechanism in a commercial LiFePO4 cell," *Journal of Power Sources*, vol. 194, pp. 541–549, Oct. 2009.

[18] L. Vichard, A. Ravey, P. Venet, F. Harel, S. Pelissier, and D. Hissel, "A method to estimate battery SOH indicators based on vehicle operating data only," *Energy*, vol. 225, p. 120235, June 2021.

[19] J. M. Lujano-Rojas, R. Dufo-López, J. L. Atencio-Guerra, E. M. Rodrigues, J. L.

Bernal-Agustín, and J. P. Catalão, "Operating conditions of lead-acid batteries in the optimization of hybrid energy systems and microgrids," *Applied Energy*, vol. 179, pp. 590–600, Oct. 2016.

[20] D. Andre, M. Meiler, K. Steiner, H. Walz, T. Soczka-Guth, and D. Sauer, "Characterization of high-power lithium-ion batteries by electrochemical impedance spectroscopy. II: Modelling," *Journal of Power Sources*, vol. 196, pp. 5349–5356, June 2011.

[21] A. Barai, "Improvement of Consistency, Accuracy and Interpretation of Characterisation Test Techniques for Li-ion Battery cells for Automotive Application,"

[22] "EV Battery Health Diagnostics System Market Report, 2034."

[23] A. S. Keefe, S. Buteau, I. G. Hill, and J. R. Dahn, "Temperature Dependent EIS Studies Separating Charge Transfer Impedance from Contact Impedance in Lithium-Ion Symmetric Cells," *Journal of The Electrochemical Society*, vol. 166, no. 14, pp. A3272–A3279, 2019.

[24] J. Zhu, X. Lai, Z. Zhu, P. Ke, Y. Zheng, X. Tang, X. Li, Y. Yuan, H. Chong, C. Yan, Y. Wang, Y. Lin, X. Zhou, and Y. Chen, "Online generation of full-frequency electrochemical impedance spectra for Lithium-ion batteries using early-stage partial relaxation voltage curve," *eTransportation*, vol. 26, p. 100482, Dec. 2025.

[25] D. A. Howey, P. D. Mitcheson, V. Yufit, G. J. Offer, and N. P. Brandon, "Online Measurement of Battery Impedance Using Motor Controller Excitation," *IEEE Transactions on Vehicular Technology*, vol. 63, pp. 2557–2566, July 2014.

[26] Y. Duan, J. Tian, J. Lu, C. Wang, W. Shen, and R. Xiong, "Deep neural network battery impedance spectra prediction by only using constant-current curve," *Energy Storage Materials*, vol. 41, pp. 24–31, Oct. 2021.

[27] Y. Che, J. Guo, Y. Zheng, D.-I. Stroe, W. Liu, X. Hu, and R. Teodorescu, "Unlocking Interpretable Prediction of Battery Random Discharge Capacity With Domain Adaptative Physics Constraint," *Advanced Energy Materials*, vol. 15, no. 13, p. 2405506, 2025. _eprint: https://advanced.onlinelibrary.wiley.com/doi/pdf/10.1002/aenm.202405506.

[28] J. Tian, R. Xiong, C. Chen, C. Wang, W. Shen, and F. Sun, "Simultaneous prediction of impedance spectra and state for lithium-ion batteries from short-term pulses," *Electrochimica Acta*, vol. 449, p. 142218, May 2023.

[29] G. Nusev, juričić, M. Gaberšček, J. moškon, and P. Boškoski, "Fast Impedance Measurement of Li-Ion Battery Using Discrete Random Binary Excitation and Wavelet Transform," *IEEE Access*, vol. 9, pp. 46152–46165, 2021.

[30] S. H. Park, J. Park, M.-H. Ryou, and Y. M. Lee, "Sensitivity of power of lithium-ion batteries to temperature: A case study using cylindrical- and pouch-type cells," *Journal of Power Sources*, vol. 465, p. 228238, July 2020.

[31] S. Micari, S. Foti, A. Testa, S. D. Caro, F. Sergi, L. Andaloro, D. Aloisio, S. G. Leonardi, G. Napoli, S. Micari, S. Foti, A. Testa, S. D. Caro, F. Sergi, L. Andaloro, D. Aloisio, S. G. Leonardi, and G. Napoli, "Effect of WLTP CLASS 3B Driving Cycle on Lithium-Ion Battery for Electric Vehicles," *Energies*, vol. 15, Sept. 2022. Company: Multidisciplinary Digital Publishing Institute Distributor: Multidisciplinary Digital Publishing Institute Institution: Multidisciplinary Digital Publishing Institute Label: Multidisciplinary Digital Publishing Institute Publisher: publisher.

[32] J. Kühlwein, "Driving resistances of light-duty vehicles in Europe: present Situation, trends, and scenarios for 2025,"

[33] E. Por, M. van Kooten, and V. Sarkovic, "Nyquist–Shannon sampling theorem,"

[34] M. Dubarry, C. Truchot, and B. Y. Liaw, "Synthesize battery degradation modes via a diagnostic and prognostic model," *Journal of Power Sources*, vol. 219, pp. 204–216, Dec. 2012.

[35] M. Lewerenz, A. Marongiu, A. Warnecke, and D. U. Sauer, "Differential voltage analysis as a tool for analyzing inhomogeneous aging: A case study for LiFePO4|Graphite cylindrical cells," *Journal of Power Sources*, vol. 368, pp. 57–67, Nov. 2017.

[36] A. Fly and R. Chen, "Rate dependency of incremental capacity analysis (dQ/dV) as a diagnostic tool for lithium-ion batteries," *Journal of Energy Storage*, vol. 29, p. 101329, June 2020.

[37] G. Seo, J. Ha, M. Kim, J. Park, J. Lee, E. Park, S. Bong, K. Lee, S. J. Kwon, S.-p. Moon, J. Choi, and J. Lee, "Rapid determination of lithium-ion battery degradation: High C-rate LAM and calculated limiting LLI," *Journal of Energy Chemistry*, vol. 67, pp. 663–671, Apr. 2022.

[38] L. Zheng, J. Zhu, D. D.-C. Lu, G. Wang, and T. He, "Incremental capacity analysis and differential voltage analysis based state of charge and capacity estimation for lithium-ion batteries," *Energy*, vol. 150, pp. 759–769, May 2018.

[39] C. S. Burrus, "Wavelets and Wavelet Transforms,"

[40] R. G. Lyons, *Understanding digital signal processing*. Upper Saddle River, NJ: Prentice Hall, 3rd ed ed., 2011.

[41] R. C. Guido, "Wavelets behind the scenes: Practical aspects, insights, and perspectives," *Physics Reports*, vol. 985, pp. 1–23, Nov. 2022.

[42] J. Lambers, "1 Introduction to Wavelet Analysis,"

[43] F. Orecchini, A. Santiangeli, and F. Zuccari, "Real Drive Well-to-Wheel Energy Analysis of Conventional and Electrified Car Powertrains," *Energies*, vol. 13, Sept. 2020.

[44] H. P. Hsu, *Schaum's outline of theory and problems of signals and systems*. Schaum's outline series, New York, NY: McGraw-Hill, 1995.

[45] R. R. Kumar, C. Bharatiraja, K. Udhayakumar, S. Devakirubakaran, K. S. Sekar, and L. Mihet-Popa, "Advances in Batteries, Battery Modeling, Battery Management System, Battery Thermal Management, SOC, SOH, and Charge/Discharge Characteristics in EV Applications," *IEEE Access*, vol. 11, pp. 105761–105809, 2023.

A | Appendix A

This appendix collects supplementary experimental material that is not included in the main chapters for readability purposes.

A.1. Additional offline EIS measurements

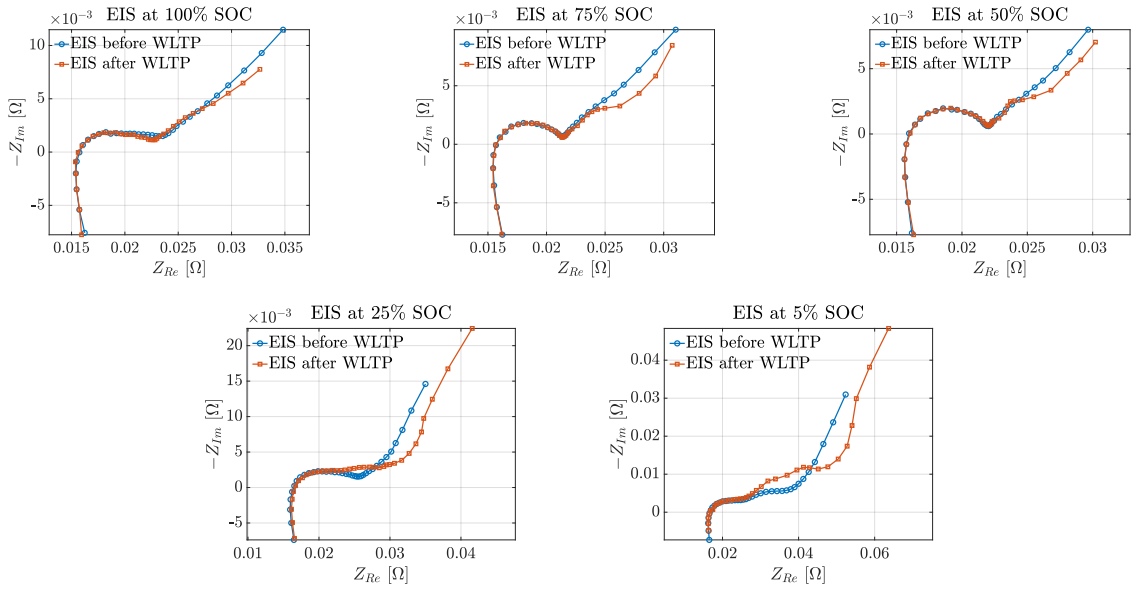

Figure A.1: Nyquist plots of the electrochemical impedance spectra measured before and after the WLTP cycle at different SOC levels (Peugeot cycle).

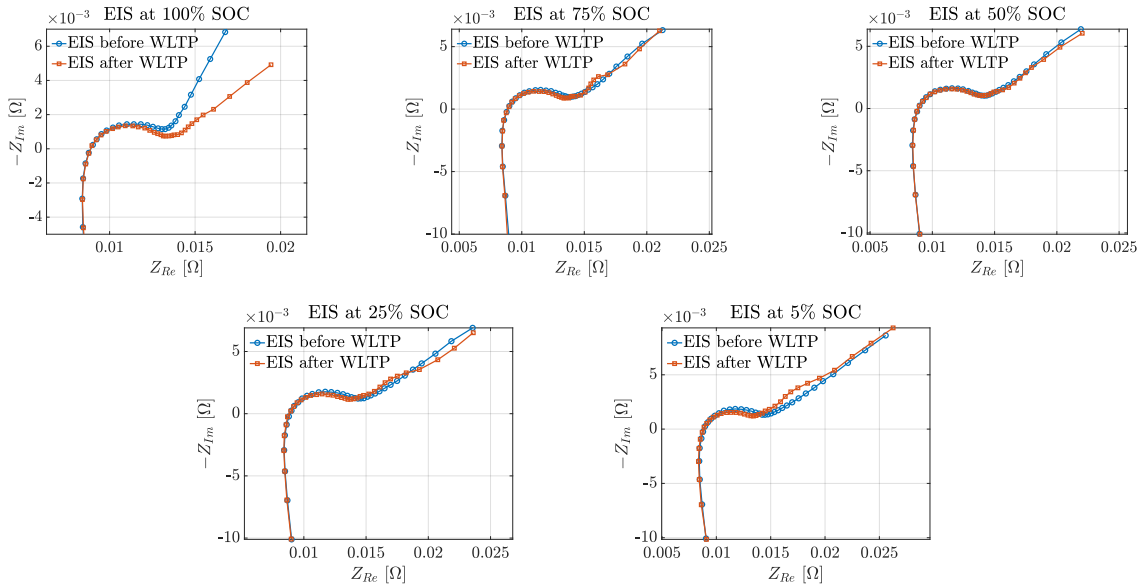

Figure A.2: Nyquist plots of the electrochemical impedance spectra measured before and after the WLTP cycle at different SOC levels (Dacia cycle).

A.2. Wavelet-based validation results

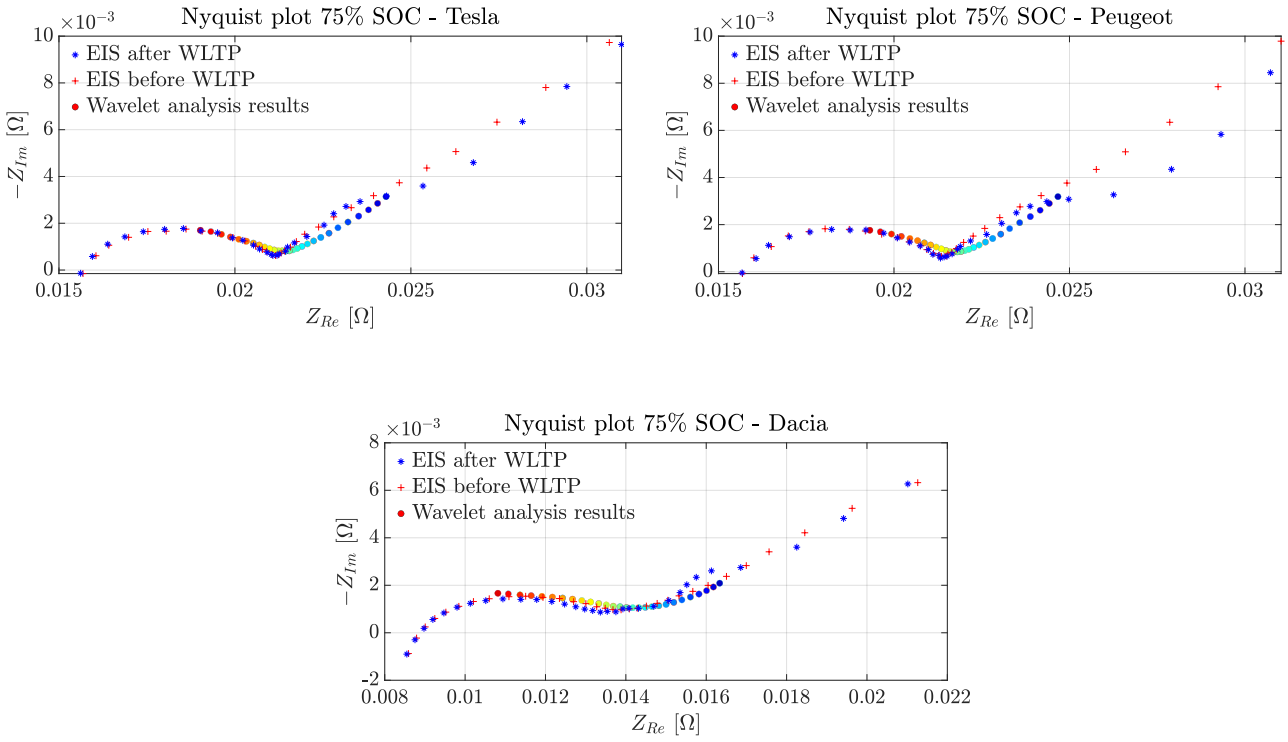

(a)

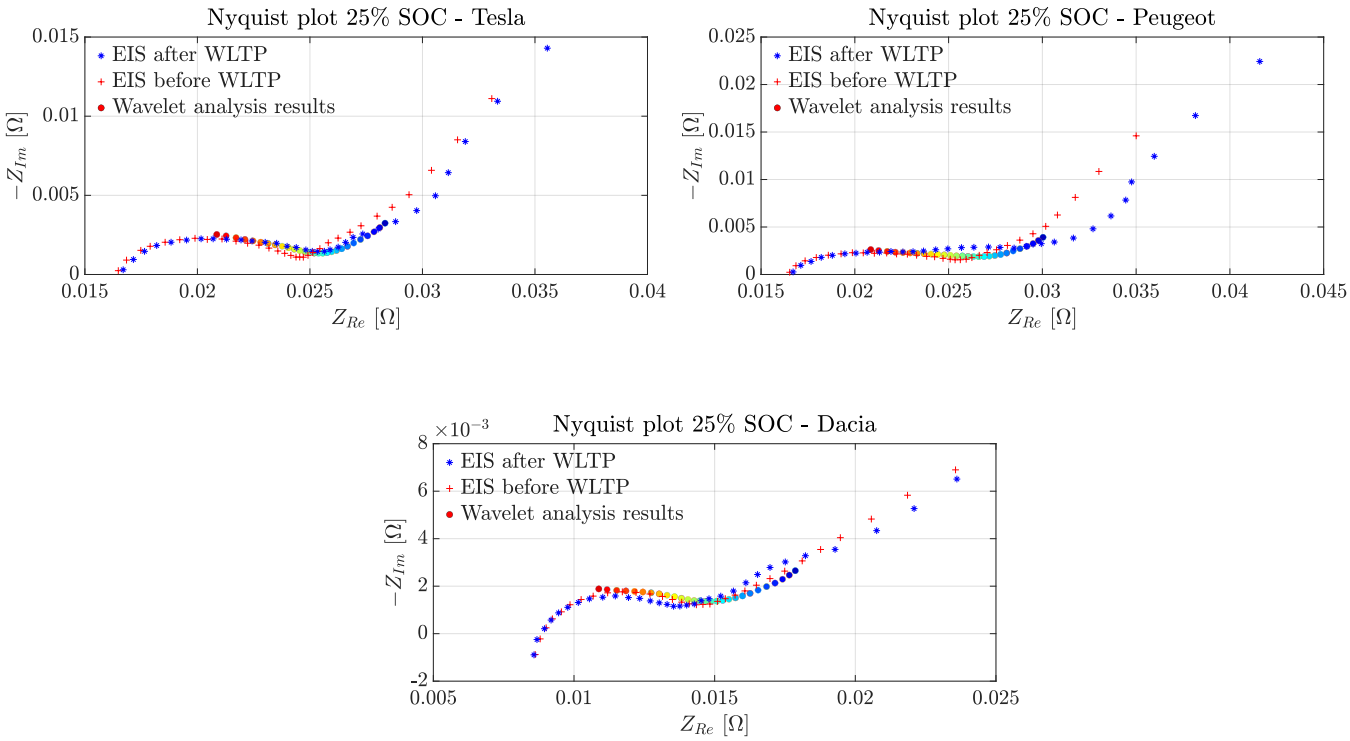

(b)

Figure A.3: Comparison of offline EIS measurements and wavelet-based online impedance estimation at different SOC levels for the three EVs: (a) 75%; (b) 25%.

List of Figures

List of Tables

List of Symbols

Variable	Description	SI unit
f	Frequency	Hz
I	Current	A
L	Inductance	L
R	Resistance	Ω
T	Temperature	K
V	Voltage	V
Z	Impedance	Ω
ϕ	Phase shift	rad
ω	Angular frequency	rad/s

Acknowledgements

I would like to express my sincere gratitude to my supervisor professor Luigi Piegari for the continuous guidance, support, and encouragement provided throughout this research work. His mentorship has been fundamental not only for the successful completion of this thesis but also for helping me develop a genuine interest and passion for the subject. His availability, insightful feedback, and constant motivation have been invaluable during this academic journey.

I would also like to sincerely thank researcher Roberta Di Fonso for her valuable contribution to the wavelet analysis study. Her support and expertise played a key role in enabling the online validation of the impedance estimation method, significantly enriching the scientific quality of this work.